ISTITUTO NAZIONALE DI FISICA NUCLEARE

Sezione di Catania

INFN/BE-96/03
30 Luglio 1996

A. Badalà, R. Barbera, A. Palmeri, G.S. Pappalardo, F. Riggi, A.C. Russo, G. Russo, R. Turrisi:

NEUTRAL PION AND HARD PHOTON PRODUCTION IN HEAVY-ION COLLISIONS AROUND 100 MeV/NUCLEON

PACS: 25.70.-z

SIS-Pubblicazioni
dei Laboratori Nazionali di Frascati

INFN – Istituto Nazionale di Fisica Nucelare
Sezione di Catania

INFN/BE–96/03
30 Luglio 1996

Neutral pion and hard photon production in heavy-ion collisions around 100 MeV/nucleon

A. Badalà[1], R. Barbera[1,2], A. Palmeri[1], G. S. Pappalardo[1],
F. Riggi[1,2], A. C. Russo[1], G. Russo[2,3] and R. Turrisi[1,2]

[1] *Istituto Nazionale di Fisica Nucleare, Sez. di Catania*
Corso Italia, 57 – I 95129 Catania, Italy

[2] *Dipartimento di Fisica dell'Università di Catania*
Corso Italia, 57 – I 95129 Catania, Italy

[3] *Istituto Nazionale di Fisica Nucleare, Laboratorio Nazionale del Sud*
Via S. Sofia, 44 – I 95123 Catania, Italy

(July 15, 1996)

Abstract

Neutral pion and hard photon energy spectra have been measured at various angles in reactions induced by a 95 MeV/nucleon ^{36}Ar beam on ^{27}Al, ^{58}Ni, ^{112}Sn, and ^{197}Au targets. Data both for pion and for hard gamma production have been compared with the results of BNV calculations. For pion production, to make a more reasonable comparison, reabsorption was taken into account on an event-by-event analysis.

I. INTRODUCTION

Pion and hard photon production has been shown to be a powerful probe of reaction dynamics in heavy-ion collisions at intermediate energies. References [1,2] and [3,4] give a good reviews of the theoretical and experimental situation for pion and high energy gamma production, respectively.

Since the discovery [5,6] of high energy gamma-ray production in heavy ion collisions, there has been a large amount of experimental [7–18] and theoretical [3,4] work directed towards the determination of the production mechanism.

The experimental data cover a wide range of target-projectile combinations and the incident beam energies range from 7.5 to 124 MeV/nucleon. Some experiments have also investigated on the impact parameter dependence of the hard photon production [19–29], showing an increase of the hard photon yield with the violence of the collision. Furthermore, the photon energy spectra tend to become softer for more peripheral reactions.

Except the first model calculations made by Vasak, Muller and Greiner [30], where it was suggested that the hard gamma production mechanism might be coherent nucleus-nucleus bremsstrahlung mainly with a quadrupole angular distribution, recent models have assumed a predominant incoherent contribution due to neutron-proton collisions and therefore with an angular distribution in the nucleon-nucleon center-of-mass that is primarily isotropic with some dipole contribution.

It is now accepted that high energy photons mainly originate from the incoherent superposition of bremsstrahlung radiation emitted during individual first chance neutron-proton collisions within the participant zone [3]. However, a recent study has demonstrated that for heavy systems hard photon emission carries also information on the stopping phase of the reaction [29].

The answer for the pions is more difficult to find, due to both experimental and theoretical problems. For example, the Hamiltonian of the πNN interaction leading to pion production is not as well defined as the electromagnetic one. Moreover, pions interact strongly with the

$75° \div 90°$	25	191 ± 9	303 ± 23	371 ± 20	610 ± 52
$75° \div 90°$	35	153 ± 8	196 ± 19	321 ± 19	464 ± 45
$75° \div 90°$	45	123 ± 7	142 ± 16	228 ± 16	321 ± 37
$75° \div 90°$	55	81 ± 6	96 ± 13	170 ± 14	221 ± 31
$75° \div 90°$	65	57 ± 5	69 ± 11	95 ± 10	138 ± 25
$75° \div 90°$	75	35 ± 4	46 ± 9	56 ± 8	114 ± 23
$75° \div 90°$	85	18 ± 3	29 ± 8	27 ± 6	88 ± 21
$75° \div 90°$	95	8 ± 2	25 ± 8	8 ± 4	31 ± 14
$75° \div 90°$	105	0.7 ± 0.7	-	2.2 ± 2.2	7 ± 7
$75° \div 90°$	115	1.8 ± 1.3	-	6 ± 4	-
$90° \div 105°$	5	129 ± 7	200 ± 18	209 ± 14	299 ± 34
$90° \div 105°$	15	215 ± 9	315 ± 23	345 ± 19	628 ± 51
$90° \div 105°$	25	182 ± 8	240 ± 20	373 ± 20	666 ± 53
$90° \div 105°$	35	143 ± 7	245 ± 21	337 ± 19	482 ± 45
$90° \div 105°$	45	116 ± 7	164 ± 17	263 ± 17	398 ± 41
$90° \div 105°$	55	62 ± 5	102 ± 13	165 ± 13	204 ± 29
$90° \div 105°$	65	51 ± 4	56 ± 10	105 ± 11	164 ± 27
$90° \div 105°$	75	26 ± 3	26 ± 7	52 ± 8	102 ± 21
$90° \div 105°$	85	12 ± 2	16 ± 6	31 ± 6	64 ± 18
$90° \div 105°$	95	7 ± 2	14 ± 6	20 ± 5	12 ± 8
$90° \div 105°$	105	3.5 ± 1.6	13 ± 6	12 ± 5	8 ± 8
$105° \div 120°$	5	140 ± 7	192 ± 18	227 ± 15	355 ± 39
$105° \div 120°$	15	216 ± 9	298 ± 23	403 ± 21	584 ± 51
$105° \div 120°$	25	177 ± 9	301 ± 24	389 ± 21	639 ± 54
$105° \div 120°$	35	135 ± 8	270 ± 23	321 ± 19	545 ± 50
$105° \div 120°$	45	100 ± 6	185 ± 19	229 ± 16	337 ± 39
$105° \div 120°$	55	66 ± 5	99 ± 14	158 ± 14	237 ± 34

$105° \div 120°$	65	40 ± 4	82 ± 13	91 ± 11	118 ± 24
$105° \div 120°$	75	22 ± 3	40 ± 9	37 ± 7	66 ± 18
$105° \div 120°$	85	12 ± 3	35 ± 9	23 ± 6	57 ± 18
$105° \div 120°$	95	2 ± 1	8 ± 5	7 ± 3	12 ± 9
$105° \div 120°$	105	3 ± 1	3 ± 3	2 ± 2	27 ± 15
$120° \div 135°$	5	138 ± 8	160 ± 18	240 ± 17	400 ± 44
$120° \div 135°$	15	205 ± 10	323 ± 26	438 ± 24	590 ± 56
$120° \div 135°$	25	188 ± 10	327 ± 28	406 ± 24	731 ± 64
$120° \div 135°$	35	159 ± 9	274 ± 26	293 ± 21	499 ± 54
$120° \div 135°$	45	100 ± 7	201 ± 22	188 ± 17	322 ± 44
$120° \div 135°$	55	60 ± 6	108 ± 17	151 ± 16	192 ± 35
$120° \div 135°$	65	39 ± 5	64 ± 13	95 ± 13	112 ± 28
$120° \div 135°$	75	23 ± 4	49 ± 12	29 ± 7	68 ± 23
$120° \div 135°$	85	10 ± 3	19 ± 8	-	18 ± 13
$120° \div 135°$	95	3 ± 1	30 ± 11	-	44 ± 22
$135° \div 150°$	5	143 ± 9	215 ± 24	277 ± 21	403 ± 51
$135° \div 150°$	15	209 ± 12	332 ± 31	453 ± 29	741 ± 74
$135° \div 150°$	25	173 ± 11	339 ± 34	414 ± 30	620 ± 72
$135° \div 150°$	35	119 ± 10	301 ± 34	266 ± 25	644 ± 77
$135° \div 150°$	45	86 ± 9	155 ± 26	263 ± 26	339 ± 59
$135° \div 150°$	55	55 ± 8	98 ± 22	105 ± 18	148 ± 41
$135° \div 150°$	65	21 ± 5	69 ± 20	61 ± 15	90 ± 35
$135° \div 150°$	75	13 ± 4	62 ± 20	52 ± 15	15 ± 15
$135° \div 150°$	85	2 ± 2	19 ± 11	26 ± 11	32 ± 23
$135° \div 150°$	95	4 ± 3	-	-	26 ± 26
$150° \div 165°$	5	127 ± 11	181 ± 28	247 ± 26	416 ± 67
$150° \div 165°$	15	211 ± 16	371 ± 44	468 ± 39	890 ± 107

$150° \div 165°$	25	180 ± 16	322 ± 45	394 ± 40	691 ± 104
$150° \div 165°$	35	113 ± 14	166 ± 35	308 ± 38	399 ± 85
$150° \div 165°$	45	85 ± 13	170 ± 41	165 ± 32	279 ± 82
$150° \div 165°$	55	60 ± 14	98 ± 36	49 ± 20	146 ± 75
$150° \div 165°$	65	17 ± 9	46 ± 29	69 ± 26	99 ± 58
$150° \div 165°$	75	11 ± 8	26 ± 26	-	-
$165° \div 180°$	5	139 ± 21	197 ± 53	239 ± 45	583 ± 142
$165° \div 180°$	15	173 ± 25	281 ± 68	594 ± 78	889 ± 190
$165° \div 180°$	25	217 ± 32	243 ± 74	434 ± 77	533 ± 169
$165° \div 180°$	35	101 ± 24	188 ± 79	160 ± 54	216 ± 125
$165° \div 180°$	45	83 ± 37	-	229 ± 82	251 ± 185
$165° \div 180°$	55	41 ± 30	-	99 ± 72	-

TABLE VI. Parameters obtained by least-squares fits to the pion spectra for angles greater than 30°. Fits were made by formula (6) with all parameters free.

Target	σ_0 (10^5 nb/sr · MeV)	τ (MeV)	β_o
^{27}Al	1.3 ± 0.4	20.7 ± 0.4	0.11 ± 0.01
^{58}Ni	1.8 ± 0.7	21.8 ± 0.6	0.05 ± 0.02
^{112}Sn	2.2 ± 0.9	20.7 ± 0.6	0.03 ± 0.02
^{197}Au	3.4 ± 1.5	20.9 ± 0.6	0.03 ± 0.02

TABLE VII. Experimental (σ_π^{exp}) production cross section of neutral pion togheter with that calculated by BNV (see text) with (σ_π^{abs}) and without (σ_π^{BNV}) reabsorption, for ^{36}Ar beam at 95 MeV/nucleon on different targets. Columns 3 and 4 give the ratios S1=$\sigma_\pi/A_t^{2/3}$ and S2=$\sigma_\pi/(A_p^{1/3}A_t^{2/3}+A_t^{1/3}A_p^{2/3})$, respectively

Target	σ_π^{exp} (μb)	S1	S2	σ_π^{abs} (μb)	σ_π^{BNV} (μb)
^{27}Al	141	15.7	2.3	161	534
^{58}Ni	210	14.0	2.3	206	802
^{112}Sn	258	11.1	2.0	516	1951
^{197}Au	404	11.9	2.3	685	3085

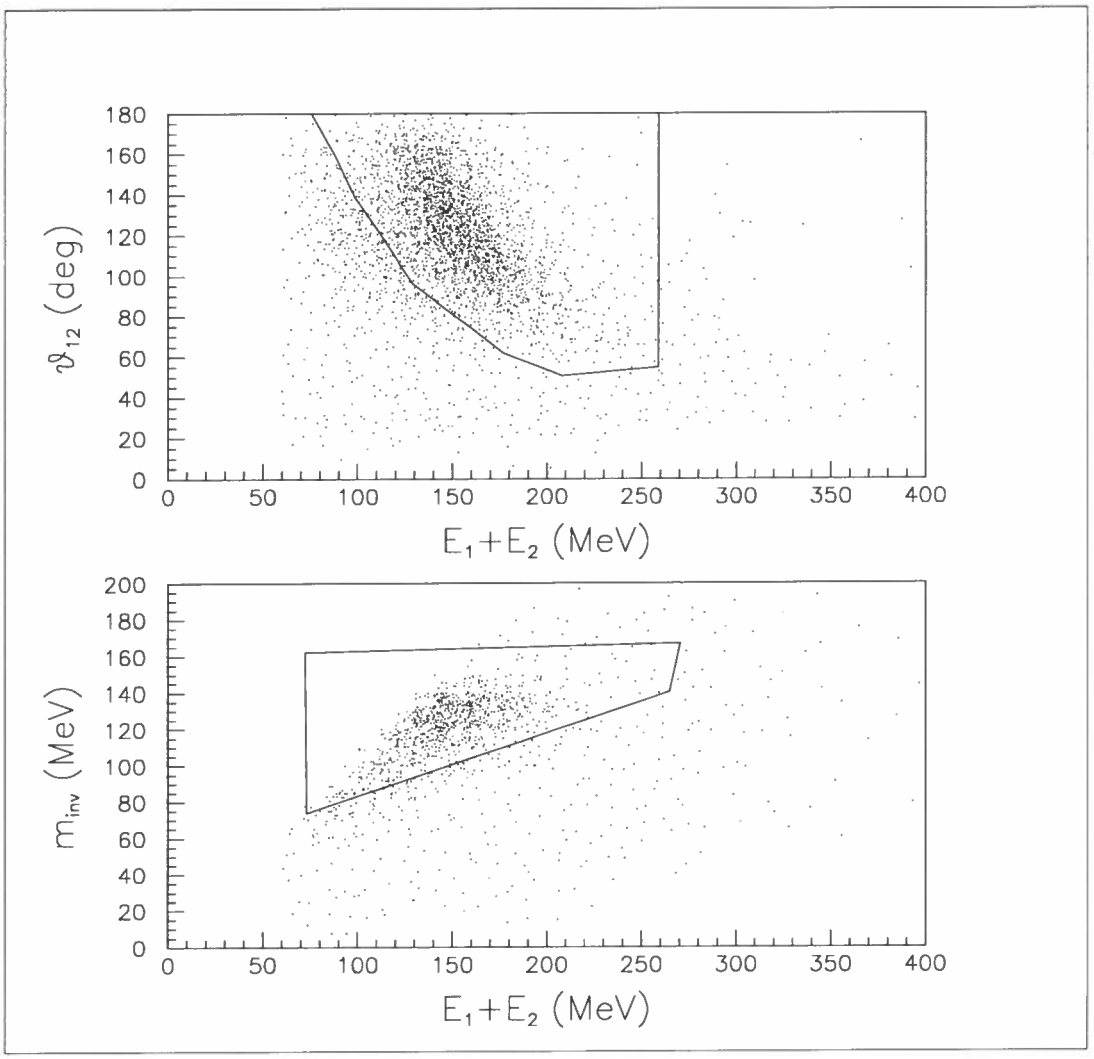

FIG. 1. Relative angle (upper panel) and invariant mass (lower panel) versus total energy distributions of the pairs of photons detected in the reaction $^{36}Ar +^{27} Al$ at 95 MeV/nucleon. In both plots, the contours define those pairs of photons coming from π° decay.

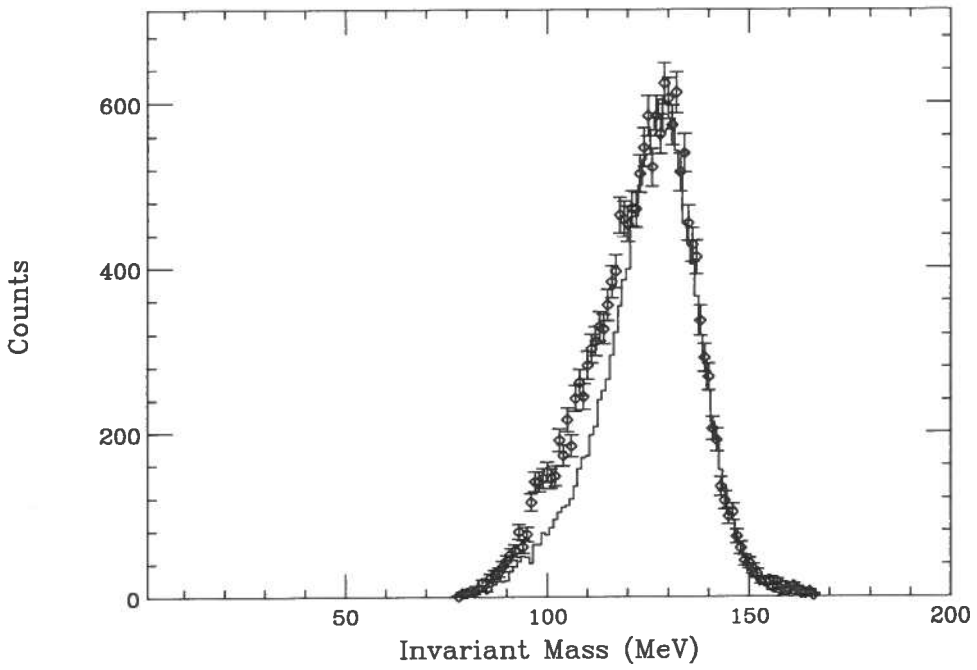

FIG. 2. Invariant mass spectrum obtained from the reaction $^{36}Ar + ^{27}Al$ at 95 MeV/nucleon (points). The solid line is the result of a GEANT3 simulation.

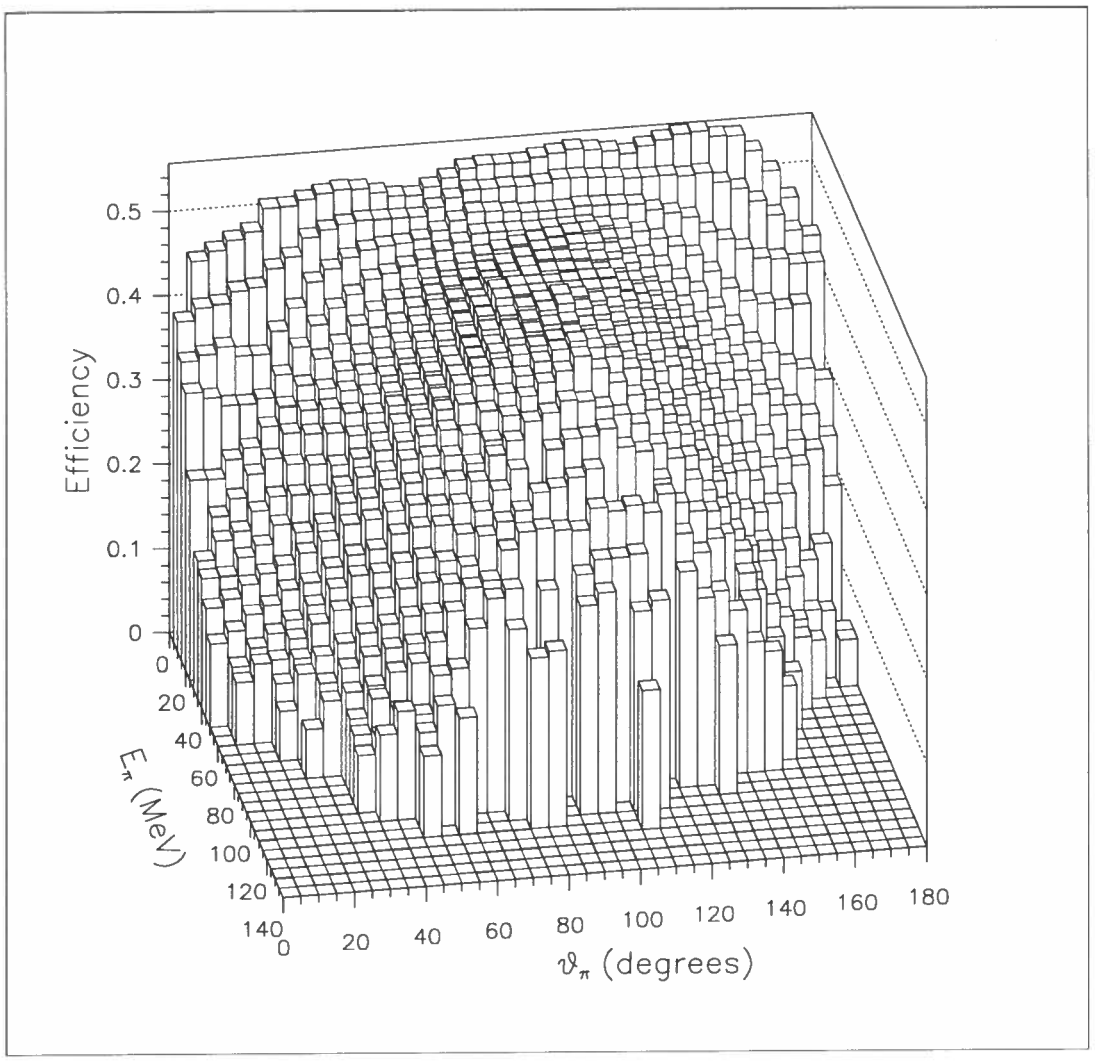

FIG. 3. Efficiency of π° as a function of pion emission angle and kinetic energy.

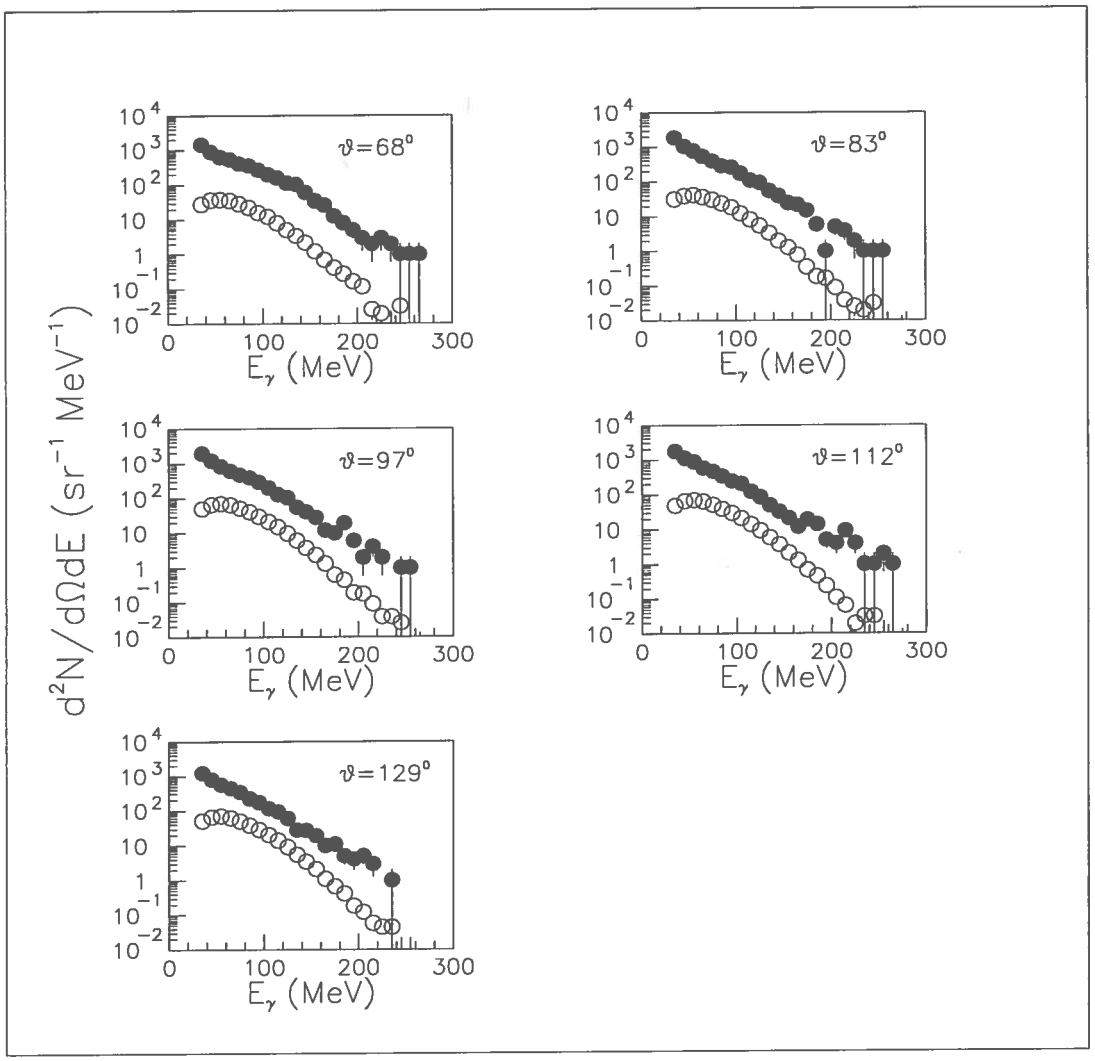

FIG. 4. Measured hard-gamma energy spectrum (full dots) and the contribution from π° decay photons, as obtained from a GEANT3 Monte Carlo simulation (empty dots) at different angles for $^{36}Ar + ^{112}Sn$ system at 95 MeV/nucleon.

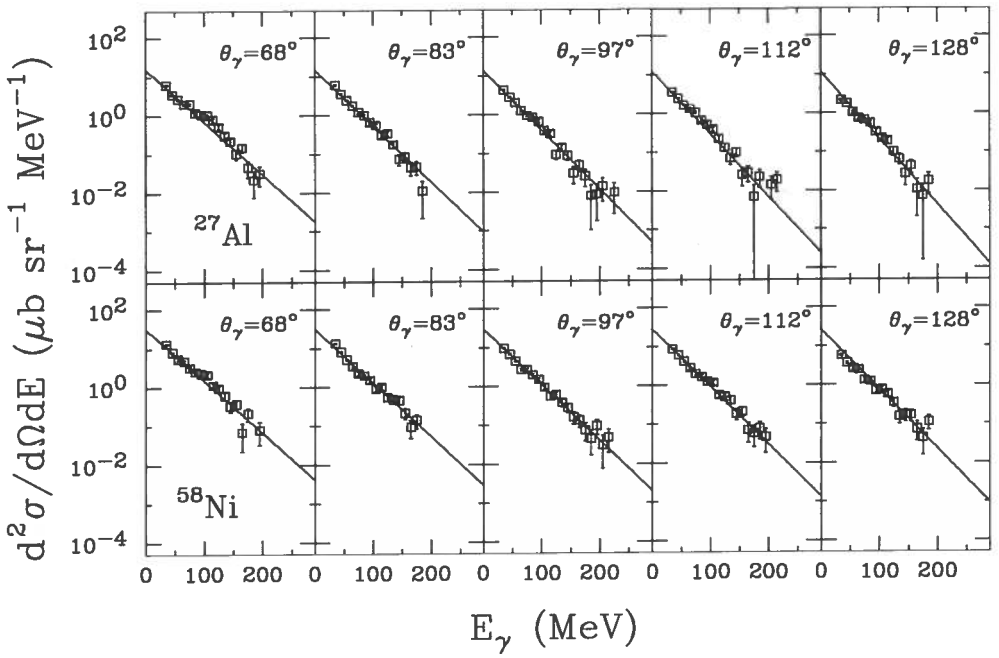

FIG. 5. Pion-subtracted hard-photon energy spectra at different angles for $^{36}Ar + ^{27}Al$ (upper panel) and $^{36}Ar + ^{58}Ni$ (lower panel) at 95 MeV/nucleon. Solid lines represent the result of the fit made by formula (4).

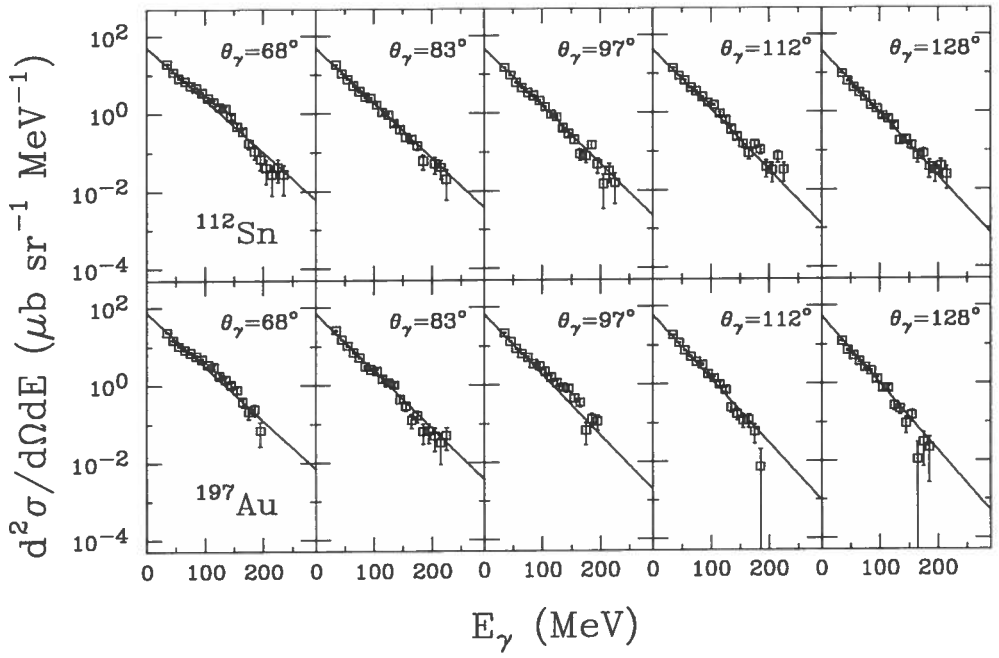

FIG. 6. As fig.5 for $^{36}Ar + ^{112}Sn$ (upper panel) and $^{36}Ar + ^{197}Au$ (lower panel) at 95 MeV/nucleon.

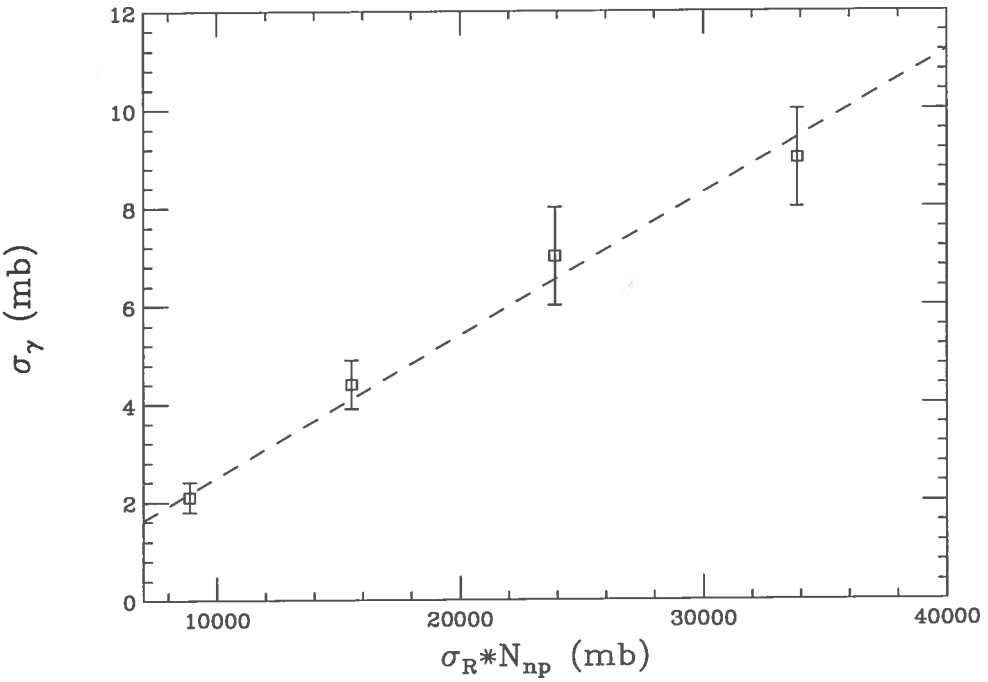

FIG. 7. Bremsstrahlung production cross section (σ_γ) versus the product of the geometrical cross section (σ_R) and the number of initial p-n collisions (N_{pn}).

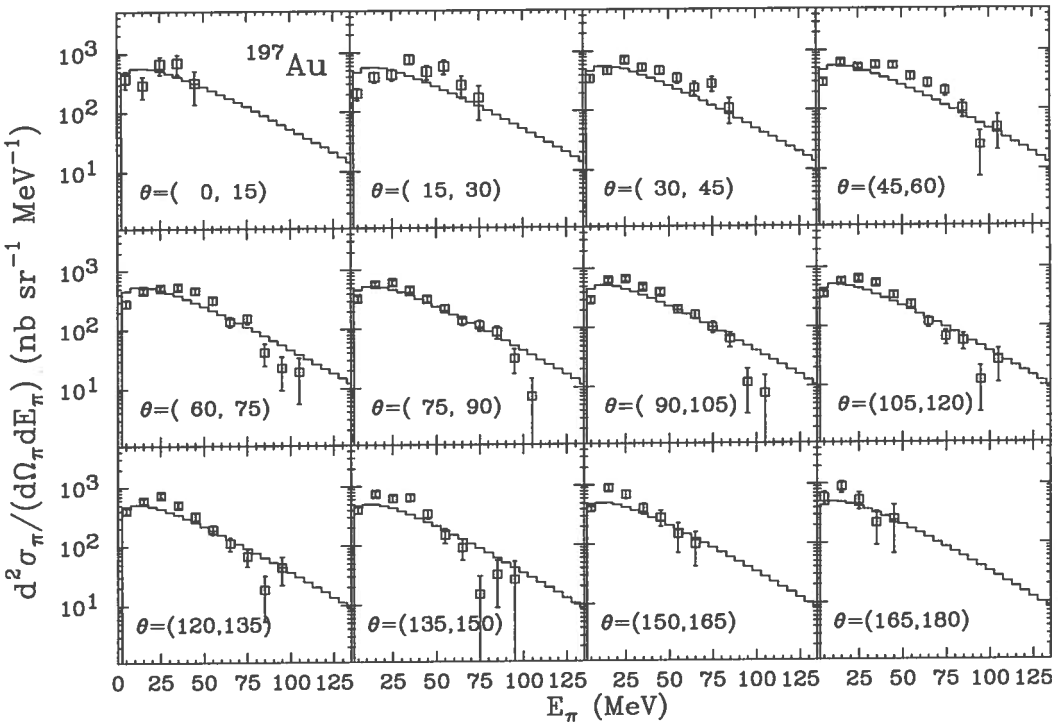

FIG. 8. Neutral pion double differential cross section for $^{36}Ar + ^{197}Au$ at 95 MeV/nucleon at different angles between 0° and 180° for steps of 15°. Solid lines represent the result of the fit made by formula (6).

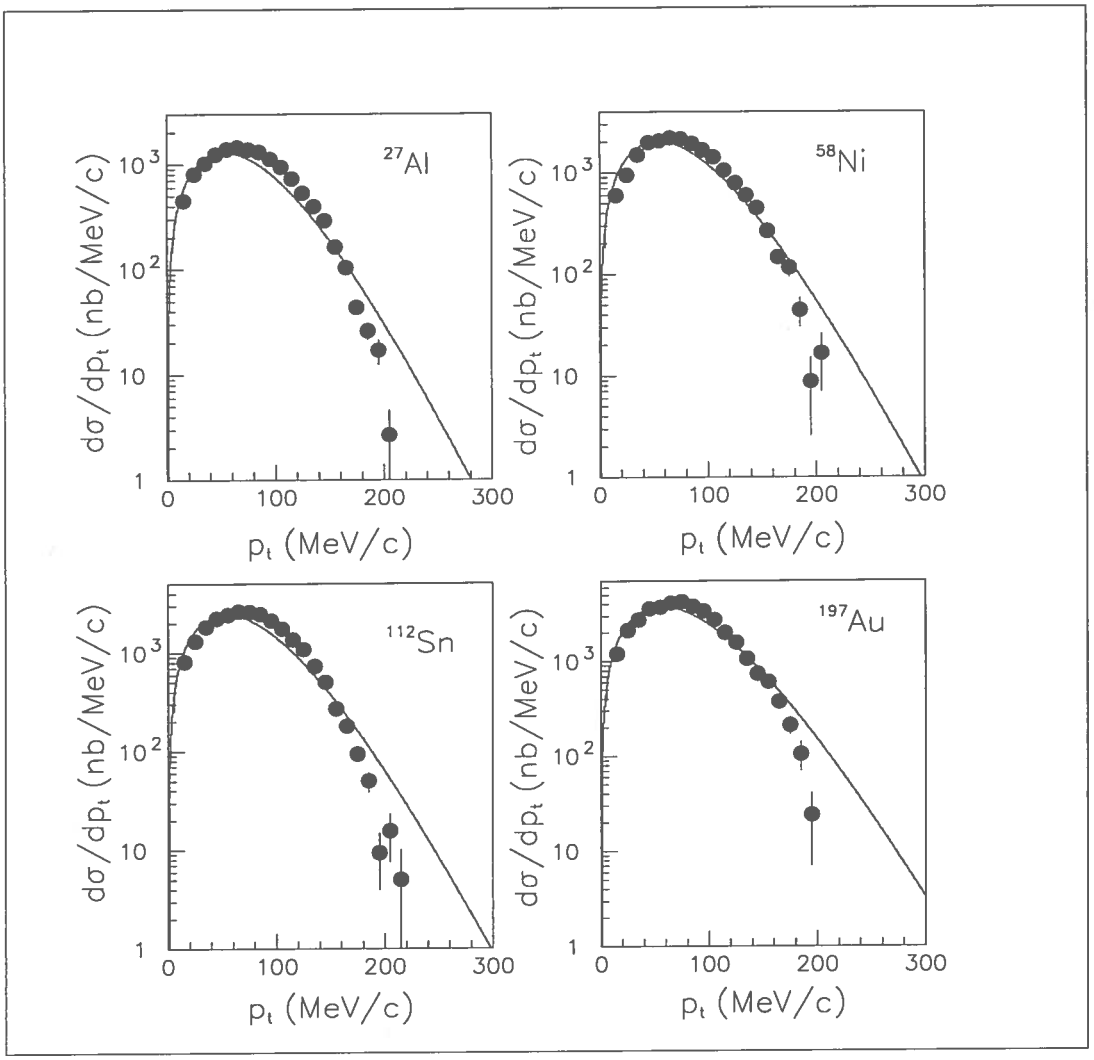

FIG. 9. Experimental pion transverse momentum distributions for ^{36}Ar at 95 MeV/nucleon on ^{27}Al, ^{58}Ni, ^{112}Sn and ^{197}Au. Solid lines represent the results of a thermal fit (see text).

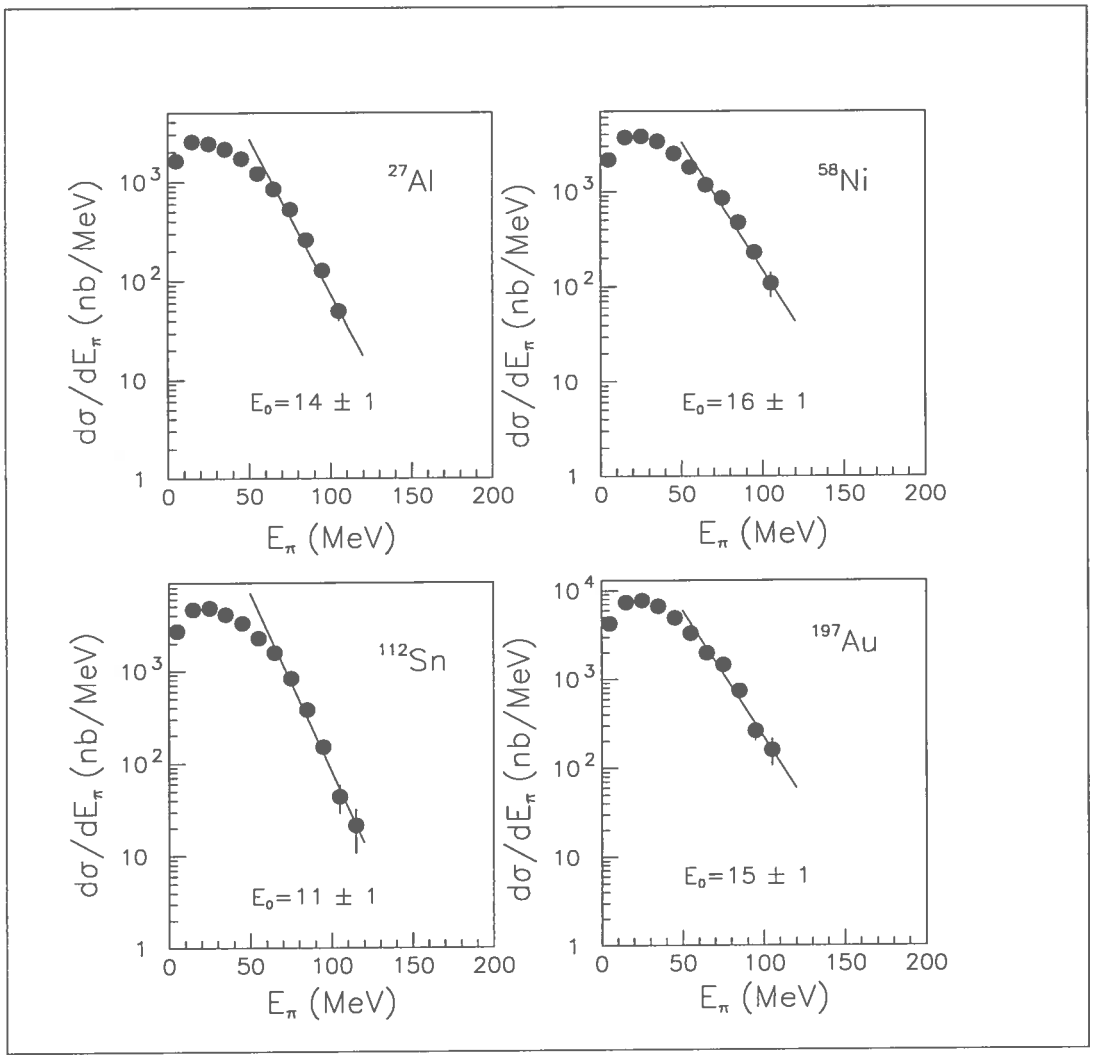

FIG. 10. Angle integrated laboratory pion kinetic energy spectra for ^{36}Ar at 95 MeV/nucleon on ^{27}Al, ^{58}Ni, ^{112}Sn and ^{197}Au. Solid lines represent the results of an exponential fit. E_0 represents the value in MeV obtained for the inverse slope parameter.

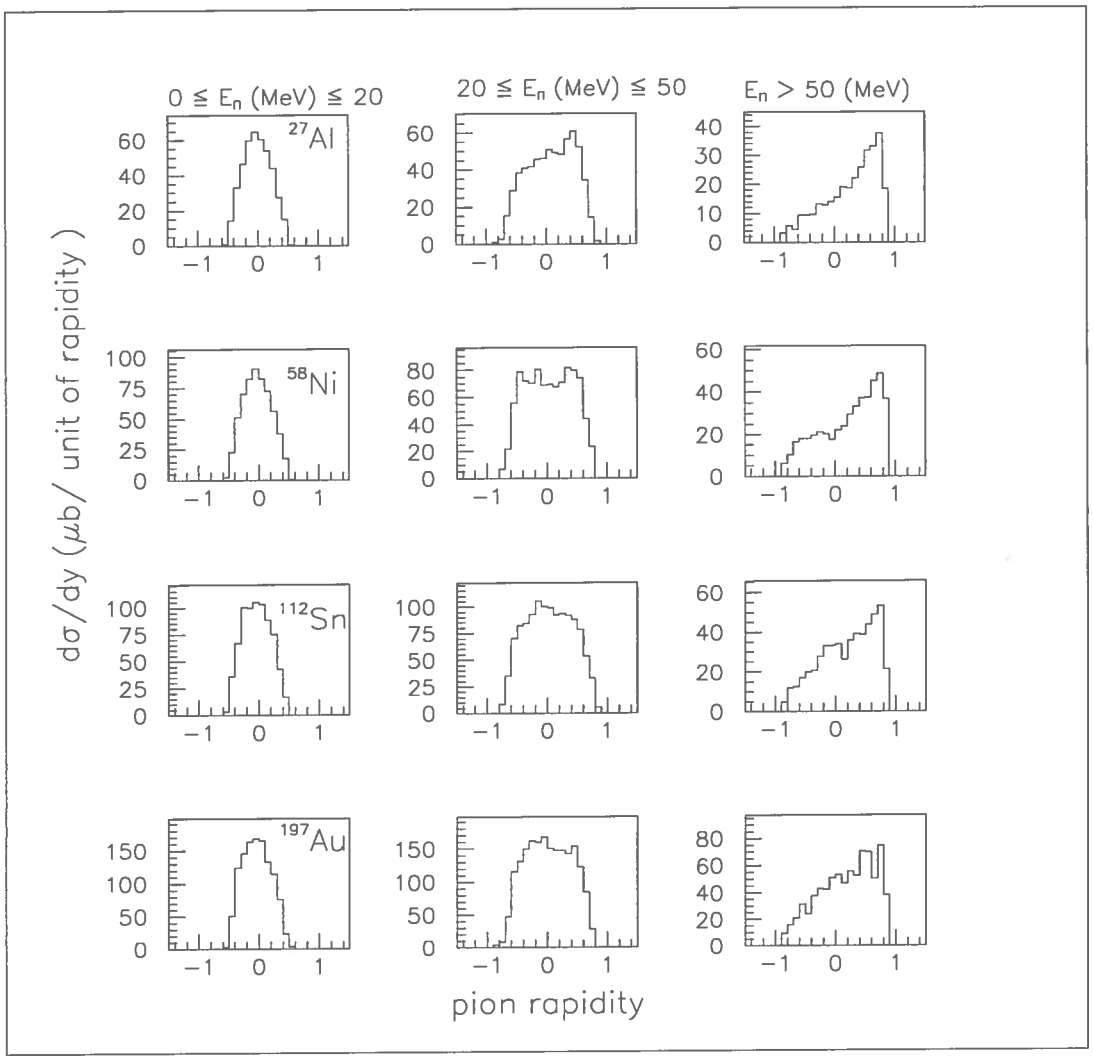

FIG. 11. Experimental pion rapidity distributions for ^{36}Ar at 95 MeV/nucleon on ^{27}Al, ^{58}Ni, ^{112}Sn and ^{197}Au for three different pion energy bins.

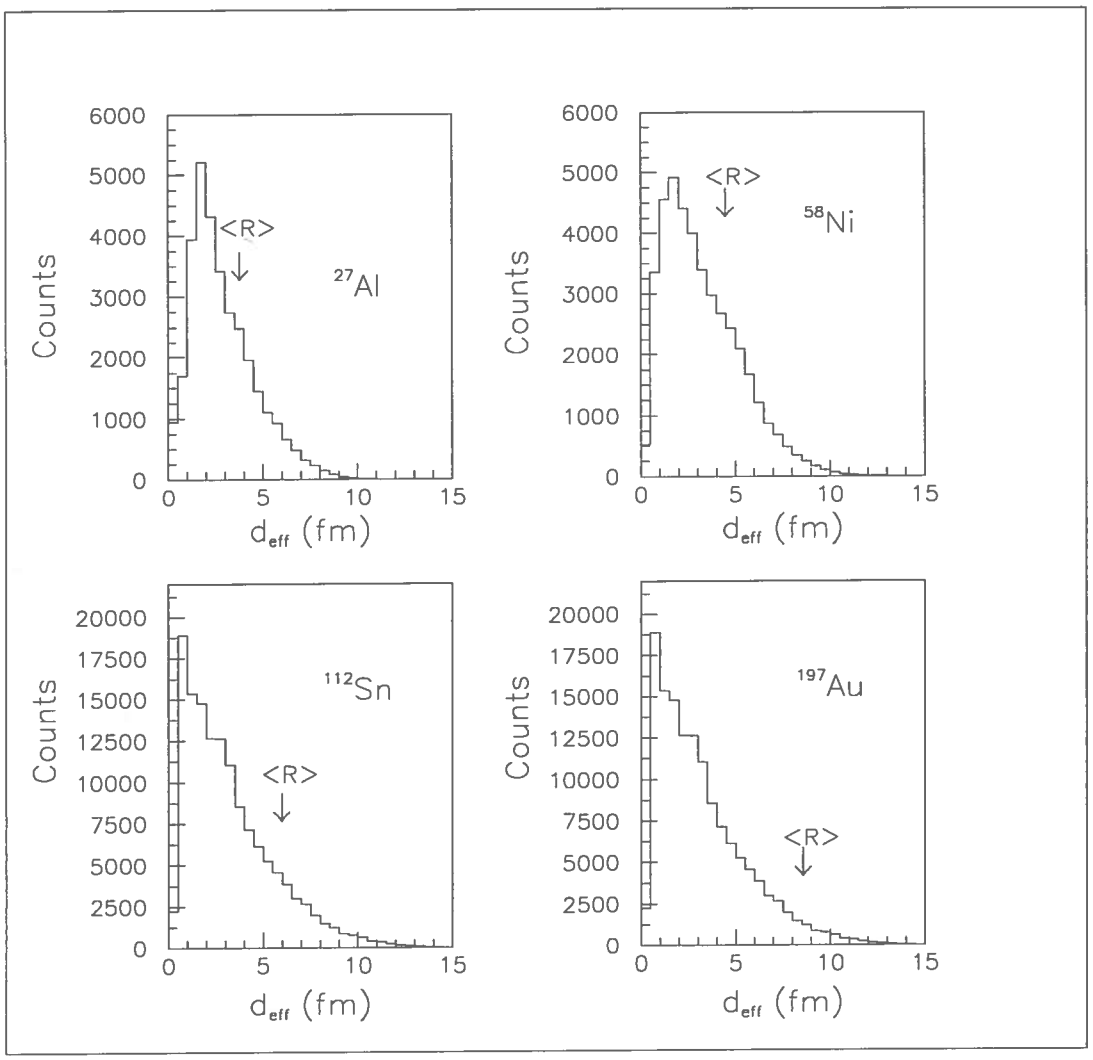

FIG. 12. Spectra of the effective traversed distance (d_{eff}) for pions in reactions induced by an ^{36}Ar beam at 95 MeV/nucleon on ^{27}Al, ^{58}Ni, ^{112}Sn, ^{197}Au targets. $< R >$ is the mean traversed distance calculated by the geometrical model of ref. [58].

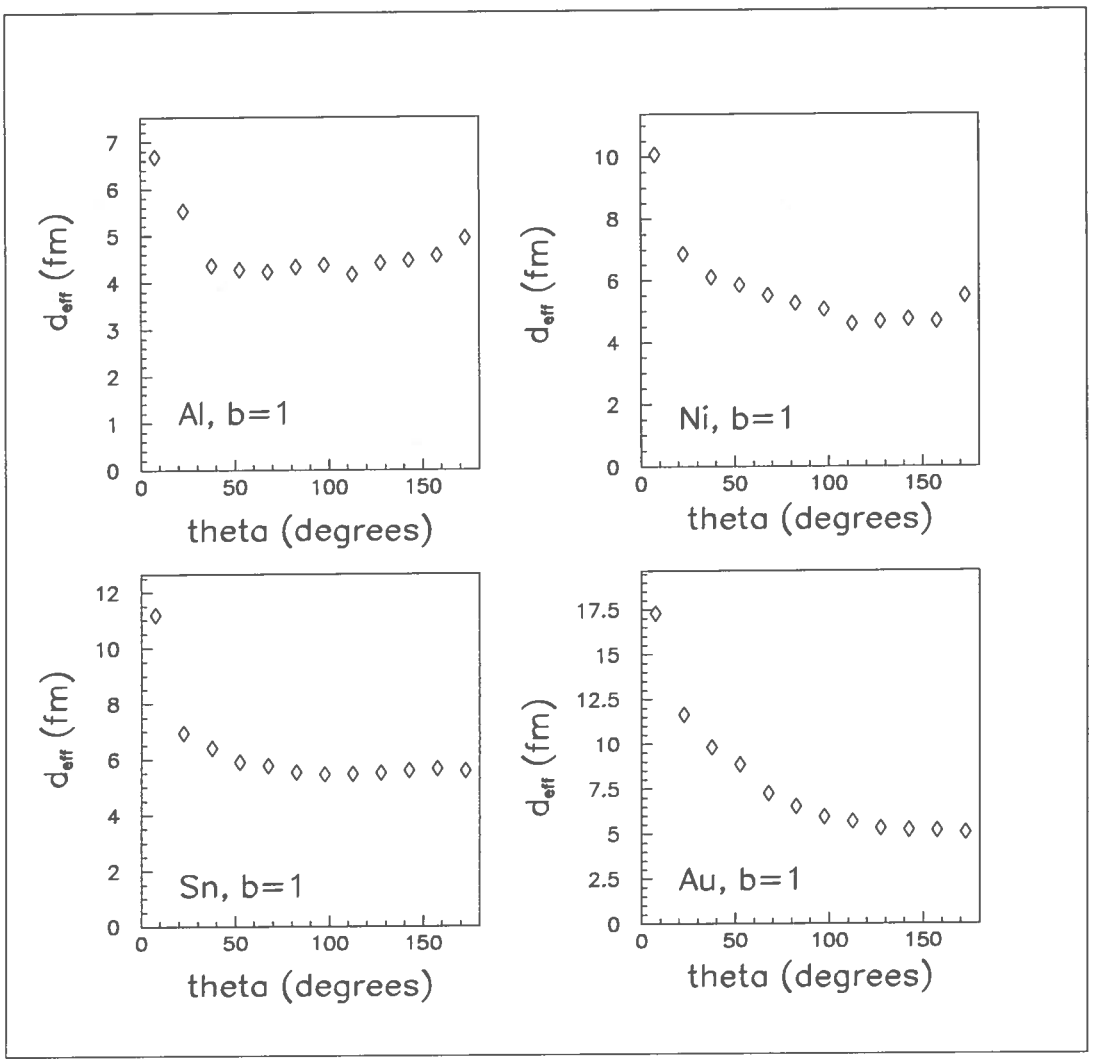

FIG. 13. The effective traversed distance (d_{eff}) as a function of the emission angle for $^{36}Ar +^{27} Al$, $^{36}Ar +^{58} Ni$, $^{36}Ar +^{112} Sn$ and $^{36}Ar +^{197} Au$ systems at 95 MeV/nucleon. Calculations were made for b=1.

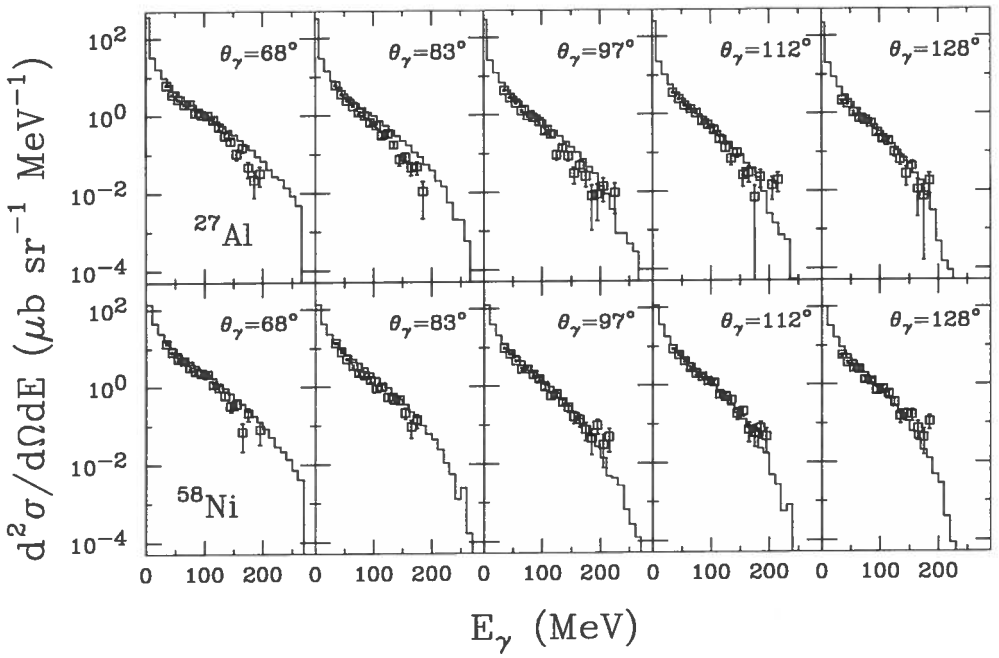

FIG. 14. Pion-subtracted hard-photon energy spectra at different angles for $^{36}Ar+^{27}Al$ (upper panel) and $^{36}Ar+^{58}Ni$ (lower panel) at 95 MeV/nucleon.The histograms are the prediction of BNV calculations (see text).

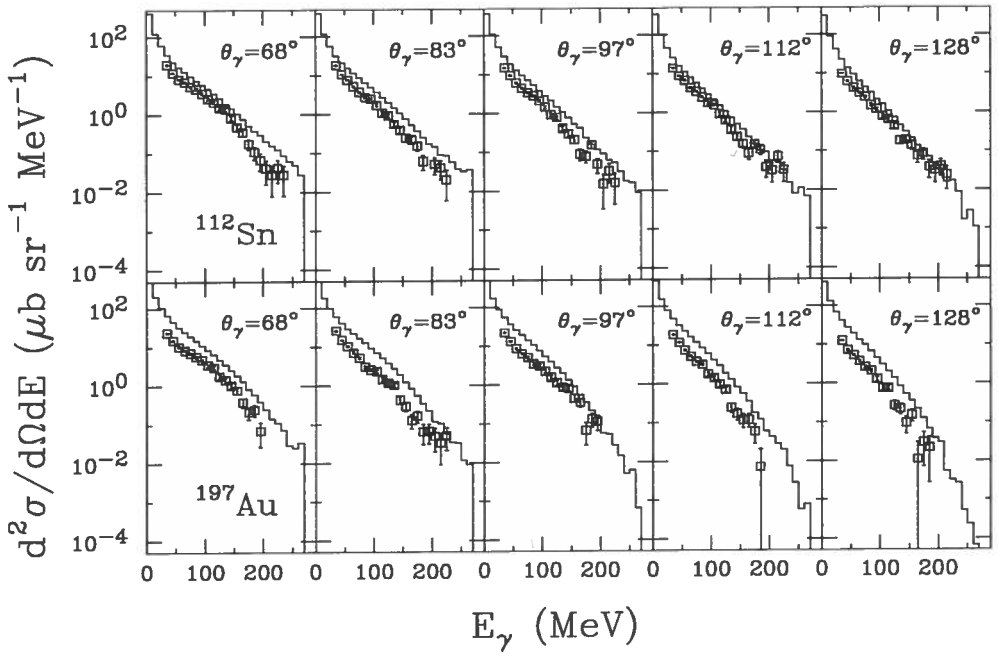

FIG. 15. As fig.14 for $^{36}Ar + ^{112}Sn$ (upper panel) and $^{36}Ar + ^{197}Au$ (lower panel) at 95 MeV/nucleon.

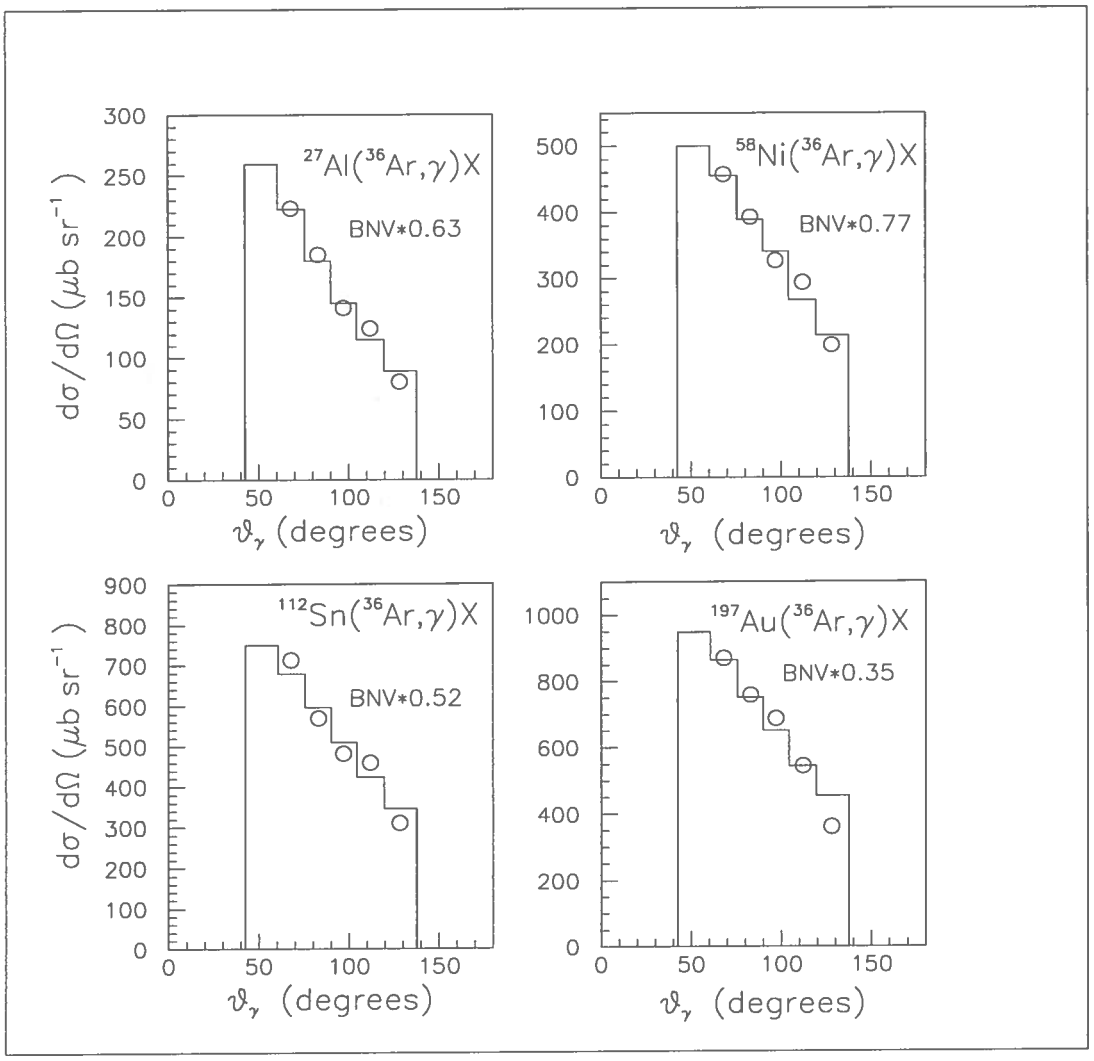

FIG. 16. Hard-gamma ($E_\gamma \geq 30$ MeV) angular distribution measured for a 95 MeV/nucleon ^{36}Ar beam on ^{27}Al, ^{58}Ni, ^{112}Sn and ^{197}Au targets. The histograms are the prediction of BNV calculations (see text). Calculations are normalized to the area of the experimental data.

for both the emitted particles we utilized the same Skyrme mean field giving a compressibility of 200 MeV.

The elementary photon production cross section was obtained by the classical theory of bremsstrahlung applied to n-p scattering. The so-called "internal radiation" from the Feynman diagrams was classically evaluated in the charged one-pion exchange hypothesis [54]. The elementary cross sections for pion production were taken from the parametrization of Ver West and Arndt [55].

In case of pions, final state effects play an important role in modifying the shape of the observed energy spectra and angular distributions. Pion reabsorption was frequently taken into account in a semiempirical way, introducing an attenuation factor $P = exp(- < R > /\lambda_\pi)$, where $< R >$ is the average path which a pion has to traverse to escape from the nuclear matter and λ_π denotes the average mean free path. Usually $< R >$ was calculated in a simple geometrical model [56], in which pions are emitted uniformly and isotropicaly from the overlap region of the two colliding nuclei. Recently, calculating an average pion path within the nuclear medium according to the model of ref. [56] and assuming the slope of the π° transverse momentum spectrum independent on the absorption, a pion absorption mean free path depending on the pion energy was successfully extracted from the data for the reaction $^{197}Au(^{144}Xe, \pi^\circ)X$ at 44 MeV/nucleon [58].

In this work we try to treat pion reabsorption in a consistent way, taking into account event-by-event the energy of the pion and the position where it is produced. Therefore, we evaluate for each event an effective distance that the pion has to travel to emerge from the nuclear region assuming it moves on a straight line determined by its momentum versor $\hat{p}_\pi$:

$$d_{eff}(\vec{r}_\pi, \hat{p}_\pi, t) = \frac{1}{\rho_0} \int_0^{+\infty} \rho(\vec{r}_\pi + \hat{p}_\pi s, t) ds \tag{8}$$

where $(\vec{r}_\pi, t)$ are the pion production space-time coordinates, s is the length of the pion path during the time t, ρ is the actual density of the nuclear matter at the time the pion is created, and ρ_0 the saturation value for the normal nuclear matter. Then, whenever the pion is created, the escape pion probability is calculated by $P_{esc} = \exp(-d_{eff}/\lambda_0)$

where $\lambda_0 = (\sigma_{abs}\rho_0)^{-1}$ represents the absorption mean free path in nuclear matter. For the dependence of λ_0 on the pion kinetic energy the parametrization of ref. [57] was employed.

In fig.12 the distribution for each target of the effective traversed distance d_{eff} is represented. In the figure the values of $< R >$ found following the geometrical approach of ref. [56] are also indicated. Especially for heavy targets these values are very high compared to the mean value of the distribution (about 3 fm). The effective traversed distance obviously depends on the source location. In fig. 13 d_{eff} is reported for the four targets as a function of the emission angle. Calculations were made for b=1. We note that for the Al target the distance to sort out is about the same whatever the emission angle is, on the contrary for the Au target we have a factor 2 between the forward and the backward emission. This claims for a backward source location and involve a strong forward suppression of pion emission.

B. Comparison and discussion

For hard photon production the BNV calculations previously described reproduce the energy distribution for each angle for all the targets (figs.14-15). Calculations overestimate the experimental results of about a factor 1.5 for the light targets (Al, Ni). This factor increases to 3 for the Au target. However, excluding this scaling factor, the general behaviour of data is reproduced (see fig.16).

In figs. 17-20 the energy spectra of pions for different angular regions between 0° and 180° for the four targets are shown. The solid histograms represent the prediction of the BNV calculations previously described where reabsorption was taken into account in a dynamical way. The dashed histograms in fig. 17 represent the prediction of the BNV calculations where reabsorption was taken into account by a mean attenuation factor [56]. We can see that calculating reabsorption on an event by event basis permit us to have a good agreement between data and dynamical calculations for a light system as Ar+Al, while for heavier interacting systems calculations predict a forward pion production stronger than the experimental data.

Observing Table VII we can note that the reabsorption effect notably reduce the yields of about a 70% – 80%. With these big corrections total cross sections for Al and Ni are reproduced, and there is only a factor 2 between calculated and measured ones for Sn and Au targets.

Pion production for the reactions Ar+Al, Ni, Sn, Au at 95 MeV/nucleon is concentrated around 15-25 fm/c (see fig.21) and for low impact parameters [41]. The distributions of the density plots for reactions with impact parameter b=3 are shown in figs.22 and 23 for the Ar+Al and Ar+Au systems. Regarding these figures we can see that in the time interval 15-25 fm/c the pion source (that in these pictures is equivalent to the zone of high density) is localized in the middle and in the backward zone of the interacting system for the Al and the Au target, respectively. Then distortions of the original angular distribution due to final state effects will be more important for the gold target than for the aluminum target. Moreover even if the ratio between cross sections with and without absorption changes from 0.32 to 0.33 going from forward to backward for Al target, and from 0.22 to 0.29 for Au target, this is not enough to obtain a complete agreement between data and calculations. This is clearly shown in fig.24 where the rapidity plots for Al and Au targets from experimental data and from BNV calculations with reabsorption taken into account are shown. Then it is possible that, to have a better agreement, the final state interactions have to be treated in a more consistent way, for example considering the pairing effects for reabsorption and/or taking into account the rescattering.

VI. CONCLUSION

The inclusive differential distribution of hard gamma and neutral pions has been measured by an ^{36}Ar beam at 95 MeV/nucleon on four targets, spanning a wide range of masses. Detector response and data analysis have been modeled with Monte Carlo simulations.

Data relative to hard gamma production indicate that the probability for hard-gamma emission in a single proton-neutron collision within the nuclear medium is independent of

the target mass.

From pion data the temperature extracted by a moving source analysis was found to be equal for all the targets, a similar result was found fitting the transverse-momentum spectra. This could indicate that the excitation energy of the source, and hence also the dimension is about the same for all the interacting systems. The source velocity determined by this analysis is very low for all the systems. This is due to a complex interplay between reabsorption effects and stopping of projectile as discussed in ref. [42]. However, each analysis effectuated on pion data is affected by the final state effects that especially for heavy interacting systems play a very important role in the definition of the shape of energy spectra and angular distribution of pions.

Hard gamma data are well reproduced by a microscopic approach based on the solution of the Boltzmann-Nordheim-Vlasov equation. Also neutral pion data have been compared with the results predicted by the same dynamical model. Taking into account reabsorption effects in an event-by-event analysis where reabsorption factor is dependent on the pion energy and on the location in the nuclear medium where pion is produced permit to reproduce pion spectra for light targets. In the case of heavy interacting systems to obtain a good agreement this analysis would be improved taking into account other effects, for example, pairing effects for reabsorption and/or rescattering.

The use of a dynamical model permit to study the evolution in the space-time of the pion source and then to extract informations about the reaction dynamics. In particular we found a backward localization of the pion source for heavy interacting systems, that implies a big stopping of the projectile.

In conclusion, we have shown in this paper a complete set of data for π° and hard gamma production. Their principal characteristics are in good agreement with the existing systematics. These data are rather well reproduced by BNV calculations, where for pion production reabsorption was taken into account in a dynamical way. This implies that at the bombarding energy of 100 MeV/nucleon incoherent nucleon-nucleon collisions play the main role in the production mechanism of these high energy probes.

REFERENCES

[1] P. Braun-Munzinger and J. Stachel, Ann. Rev. Nucl. Part. Sci. 37,97(1987) and references therein.

[2] I.S. Batkin, I.V. Kopytin and Yu.É. Penionzhkevich, Sov. J. Part. Nucl. 22,249(1991), and references therein.

[3] W. Cassing, V. Metag, U. Mosel and K. Niita, Phys. Rep. 188,363(1990) and references therein.

[4] H. Nifenecker and J.A. Piston, Prog. Part. Nucl. Phys. 23,271(1989) and references therein.

[5] E. Grosse, *Proceedings of the International Workshop on Gross Properties of Nuclei and Nuclear Excitation XIII, Hirschegg, Austria, 1985*, edited by H. Felmeier (Gesellschaft für Kernphysik, Technische Hochschule, Darmstadt, West Germany, 1985.

[6] K.B. Beard, W. Benenson, C. Bloch, E. Kashy, J. Stevenson, D.J. Morrissey, J. Van der Plicht, B. Sherril and J.S. Winfield, Phys. Rev. C32(1985)1111; E. Grosse, P. Grimm, H. Heckwolf, W.F.J. Müller, H. Noll, A. Oskarsson, H. Stelzer and W. Rösch, Europhys. Lett. 2,9(1986).

[7] J. Stevenson, K.B. Beard, W. Benenson, J. Clayton, E. Kashy, A. Lampis, D.J. Morrissey, M. Samuel, R.J. Smith, C.L. Tam and J.S. Winfield, Phys. Rev. Lett. 57,555(1986).

[8] M. Kwato Njock, M. Maurel, E. Monnand, H. Nifenecker, J. Pinston, F. Schussler and D. Barneoud, Phys. Lett. B175,125(1986).

[9] N. Alamanos, P. Braun-Munzinger, R.F. Freifelder, P. Paul, J. Stachel, T.C. Awes, R.L. Ferguson, F.E. Obenshain, F. Plasil and G.R. Young, Phys. Lett. B173,392(1986).

[10] R. Bertholet et al., Nucl. Phys. A474,541(1987).

[11] K. Hanold and D.J. Morrissey, Phys. Rev. C38,165(1988).

[12] J. Clayton et al., Phys. Rev. 40,1207(1989).

[13] T.K. Murakami, W. Benenson, Y. Chen, J. Clayton, E. Kashy, J. Stevenson, C.L. Tam, K. Hanold and M. Mohar, Phys. Rev. C40,2079(1989).

[14] C.L. Tam et al., Phys. Rev. C39,1371(1989).

[15] G. Breitbach et al., Phys. Rev. C40,2893(1989).

[16] R.J. Vojtech, R. Butsch, V.M. Datar, M.G. Herman, R.L. McGrath, P. Paul and M. Thoennessen, Phys. Rev. C40,2441(1989).

[17] C.A. Gossett, J.A. Behr, S.J. Luke, B.T. McLain, D.P. Rosenzweig, K.A. Snover and W.T. Hering, Phys. Rev. 42,1800(1990).

[18] S.J. Luke, R. Vandenbosch, W. Benenson, J. Clayton, K. Joh, D. Krofcheck, T.K. Murakami and J.D. Stevenson, Phys. Rev. C47,1211(1993).

[19] R. Hingmann et al., Phys. Rev. Lett. 58,759(1987).

[20] J.J. Gaardhøje et al., Phys. Rev. Lett. 59,1409(1987).

[21] A.R. Lampis et al., Phys. Rev. C38,1961(1988).

[22] M. Kwato Njock, M. Maurel, E. Monnand, H. Nifenecker, P. Perrin, J.A. Pinston, F. Schussler and Y. Shutz, Nucl. Phys. A489,368(1988).

[23] N. Herrmann et al., Phys. Rev. Lett. 60,1630(1988).

[24] L.G. Sobotka et al., Phys. Rev. C44,2257(1991).

[25] T. Reposeur et al., Phys. Lett. B276,418(1992).

[26] S. Riess et al., Phys. Rev. Lett. 69,1504(1992).

[27] E. Migneco et al., Phys. Lett. B298,46(1993).

[28] G. Martinez et al.,Phys. Lett. B334,23(1994).

[29] A. Schubert et al., Phys. Rev. Lett. 72,1608(1994).

[30] D. Vasak, B. Muller and W. Greiner, J. Phys. G11,1309(1985).

[31] G. Sanouillet et al., Nuovo Cim. 99,875(1988).

[32] A. Badalá et al., Phys. Rev. C43,190(1991).

[33] T. Suzuki et al., Phys. Lett. B257,27(1991).

[34] C. Moisan et al., Nucl. Phys. A537,667(1992).

[35] A. Badalá et al., Phys. Rev. C47,231(1993).

[36] W. Waters et al., Nucl. Phys. A564,595(1993).

[37] A. Badalá et al., Nucl. Phys. A482,511c(1988).

[38] B. Norén et al., Nucl. Phys. A489,763(1988).

[39] S. Aiello et al., Europhys. Lett. 6,25(1988).

[40] B. Erazmus et al., Nucl. Phys. A481,821(1988).

[41] A. Badalá et al., Phys. Rev. C48,2350(1993).

[42] A. Badalá, R. Barbera, A. Palmeri, G.S. Pappalardo, F. Riggi, A.C. Russo, G. Russo and R. Turrisi, Phys. Rev. C53,1782(1996).

[43] E. Migneco et al., NIM A314,31(1992).

[44] CERN Application Software Group, GEANT: Detector Description an Simulation Tool (CERN, CH, 1993).

[45] A. Badalá, R. Barbera, A. Palmeri, G.S. Pappalardo, F. Riggi and A.C. Russo, NIM A306,283(1991).

[46] A. Badalá, R. Barbera, A. Palmeri, G.S. Pappalardo, F. Riggi, A.C. Russo, G. Russo and R. Turrisi, NIM A357,443(1995).

[47] H. Nifenecker and J.P. Bondorf, Nucl. Phys. A442,478(1985).

[48] M. Abramowitz and I.A. Stegun, Handbook of Mathematical Functions, (Davies, New York, 1972).

[49] N. Noll et al.,Phys. Rev. Lett. 52,1284(1984).

[50] J. Stachel et al., Phys. Rev. C33,1420(1986).

[51] G. Bertsch and S. Das Gupta, Phys. Rep. 160,190(1988), and references therein.

[52] A. Bonasera, F. Gulminelli and J.J. Molitoris, Phys. Rep. 243,1(1993).

[53] A. Bonasera, G. Russo and H.H. Wolter, Phys. Lett. B246,337(1990).

[54] G. Russo, Nucl. Phys. A575,449(1994).

[55] B.J. Ver West and R.A. Arndt, Phys. Rev. C25,1979(1982).

[56] W. Cassing, Z. Phys. A329,487(1988).

[57] J. Hufner and M. Thies, Phys. Rev. C20,273(1979).

[58] R.S. Mayer et al., Phys. Rev. Lett. 70,904(1993).

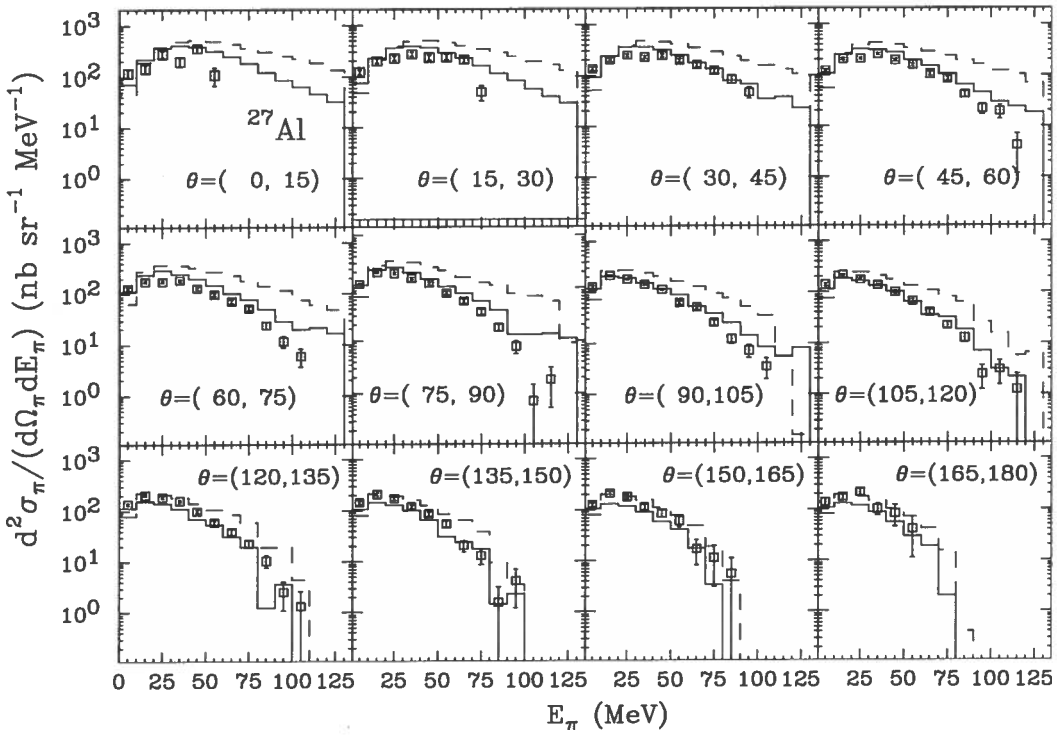

FIG. 17. Experimental (points) pion energy spectra at different detection angles and the results of a BNV dynamical calculation taking into account the effects of pion reabsorption on a event by event basis (solid histograms) for $^{36}Ar +^{27} Al$ at 95 MeV/nucleon. The dashed histograms represent the BNV calculation with reabsorption taken into account by a mean attenuation factor.

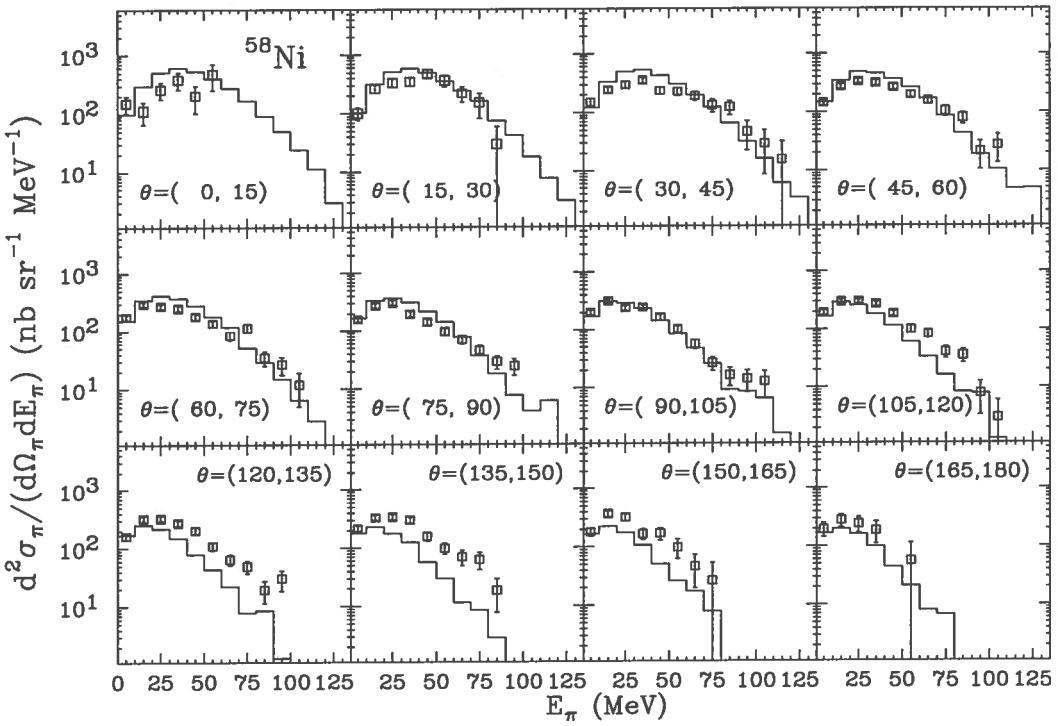

FIG. 18. As fig.17 for $^{36}Ar + ^{58}Ni$ at 95 MeV/nucleon.

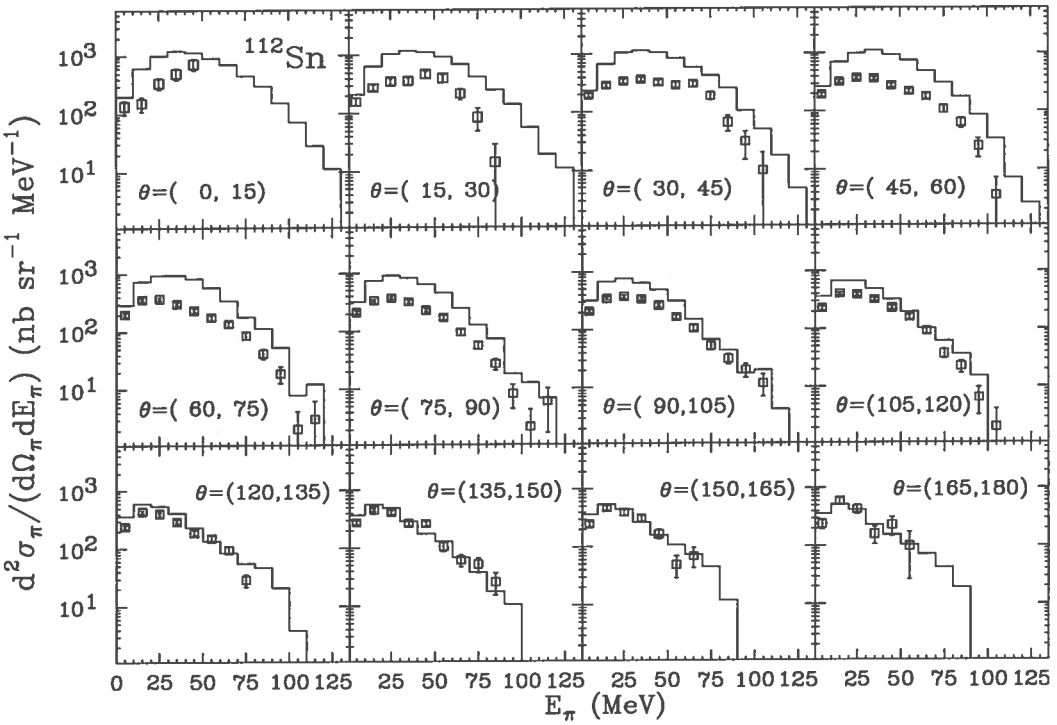

FIG. 19. As fig.17 for $^{36}Ar + ^{112}Sn$ at 95 MeV/nucleon.

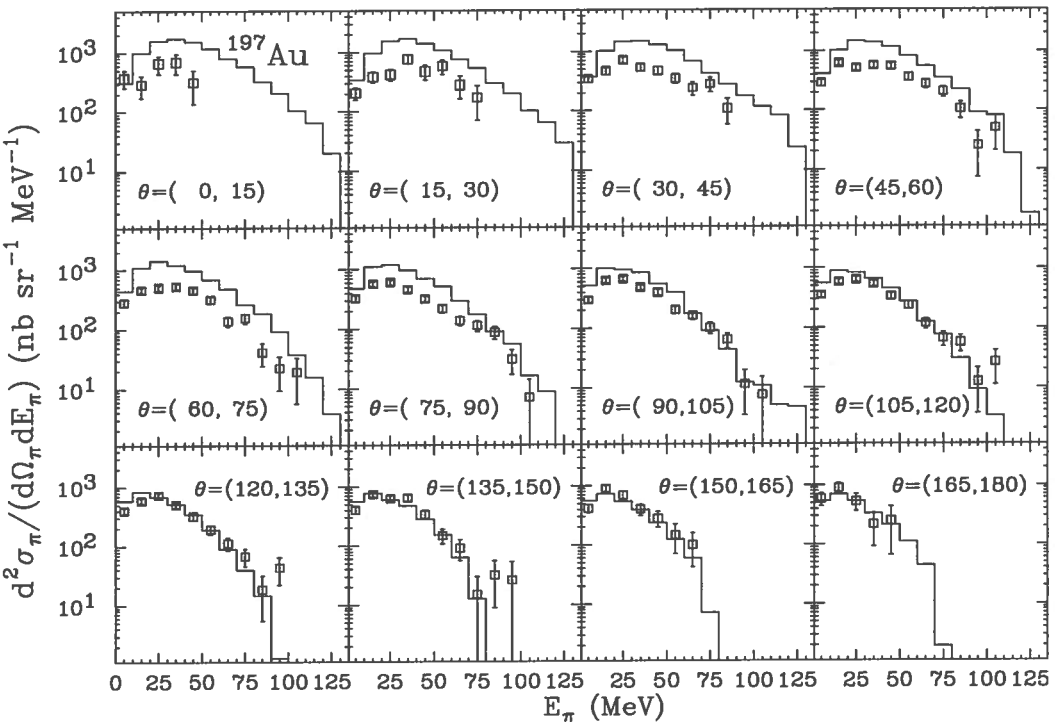

FIG. 20. As fig.17 for $^{36}Ar + ^{197}Au$ at 95 MeV/nucleon.

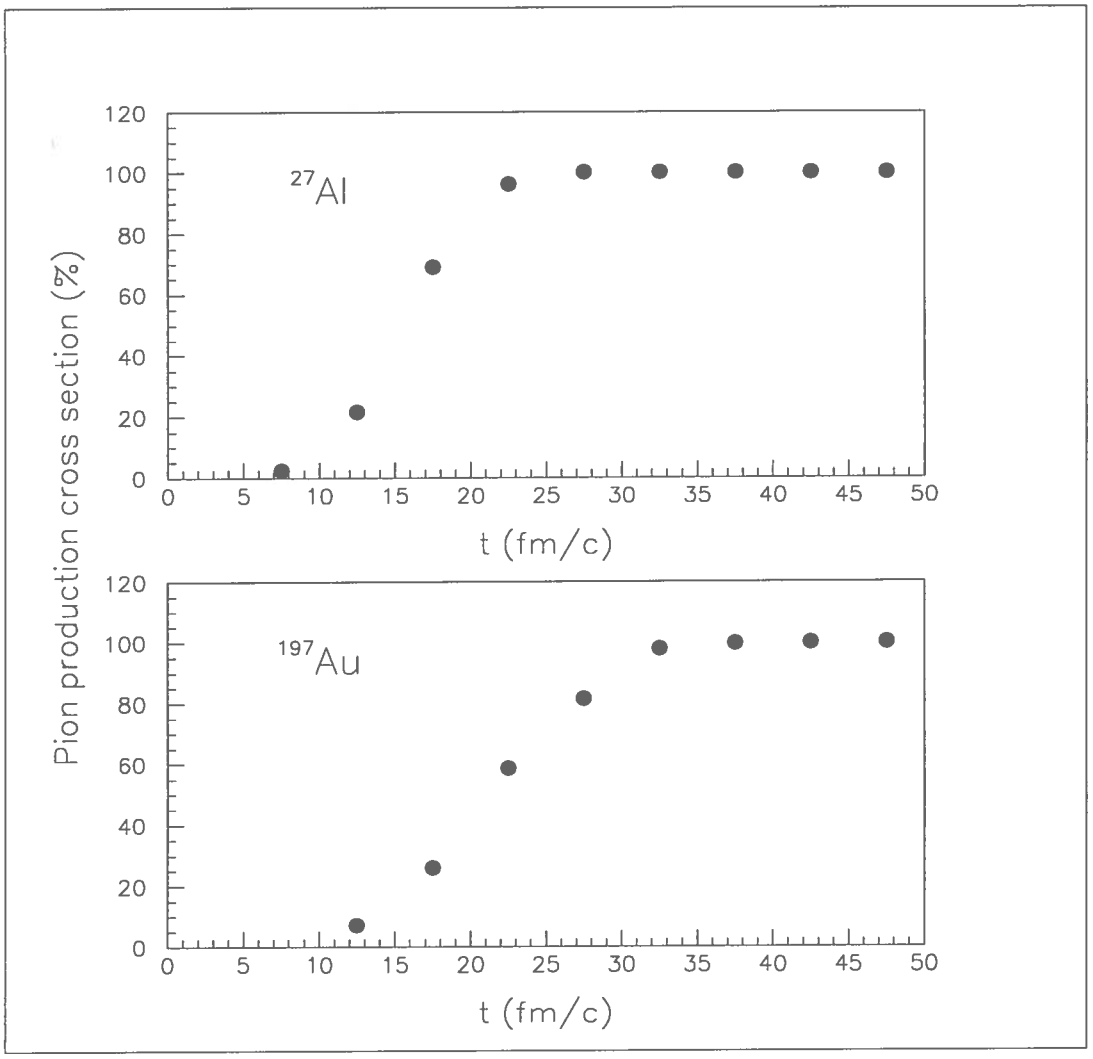

FIG. 21. Total neutral pion production cross section for $^{36}Ar+^{27}Al$ and $^{36}Ar+^{197}Au$ reactions at 95 MeV/nucleon as a function of time as predicted by BNV calculations.

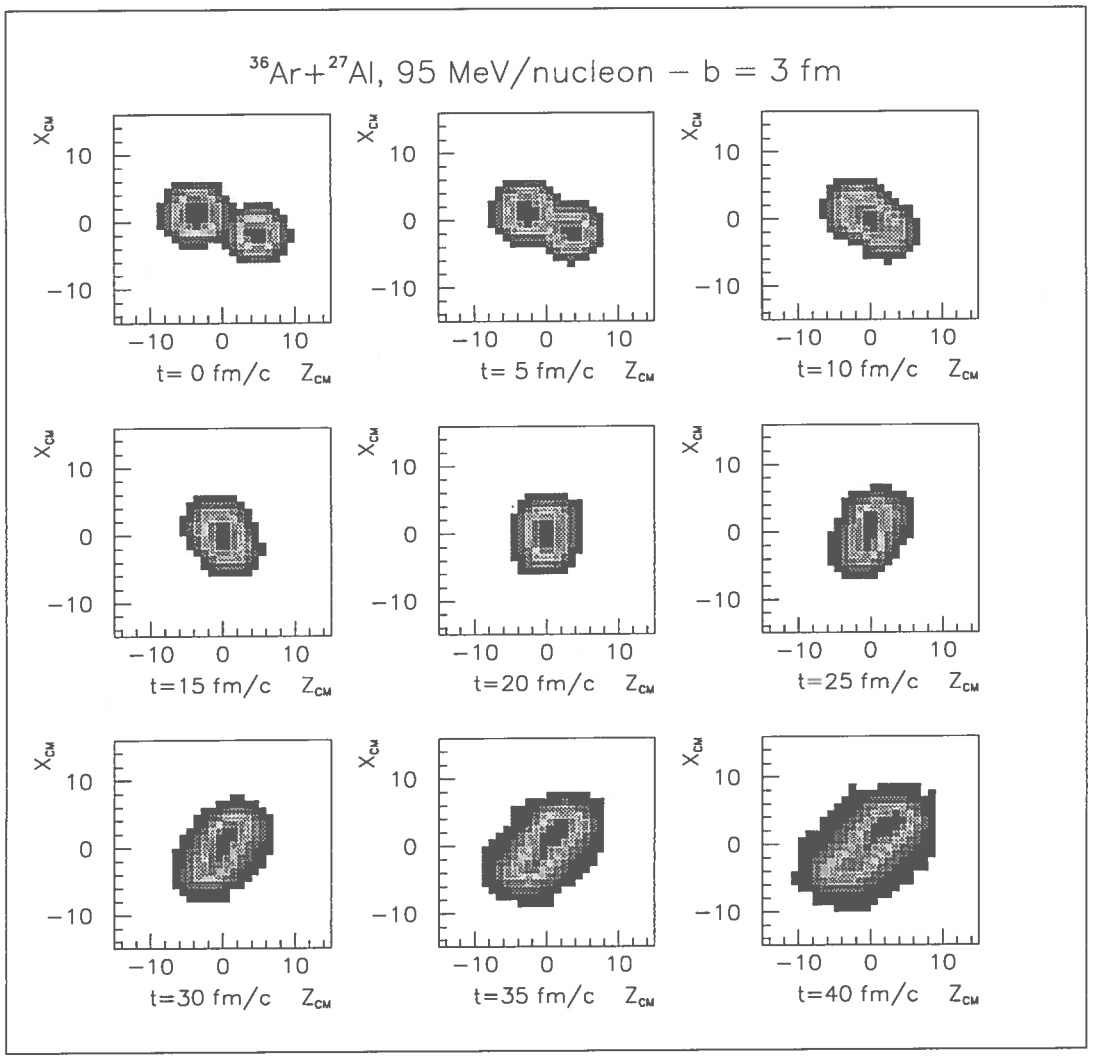

FIG. 22. Center-of-mass density distribution of $^{36}Ar + ^{27}Al$ system at 95 MeV/nucleon in the plane XZ at different time steps. The beam axis is oriented along the Z axis, the X axis is parallel to the impact parameter vector. Calculations have been performed with an impact parameter b=3 fm.

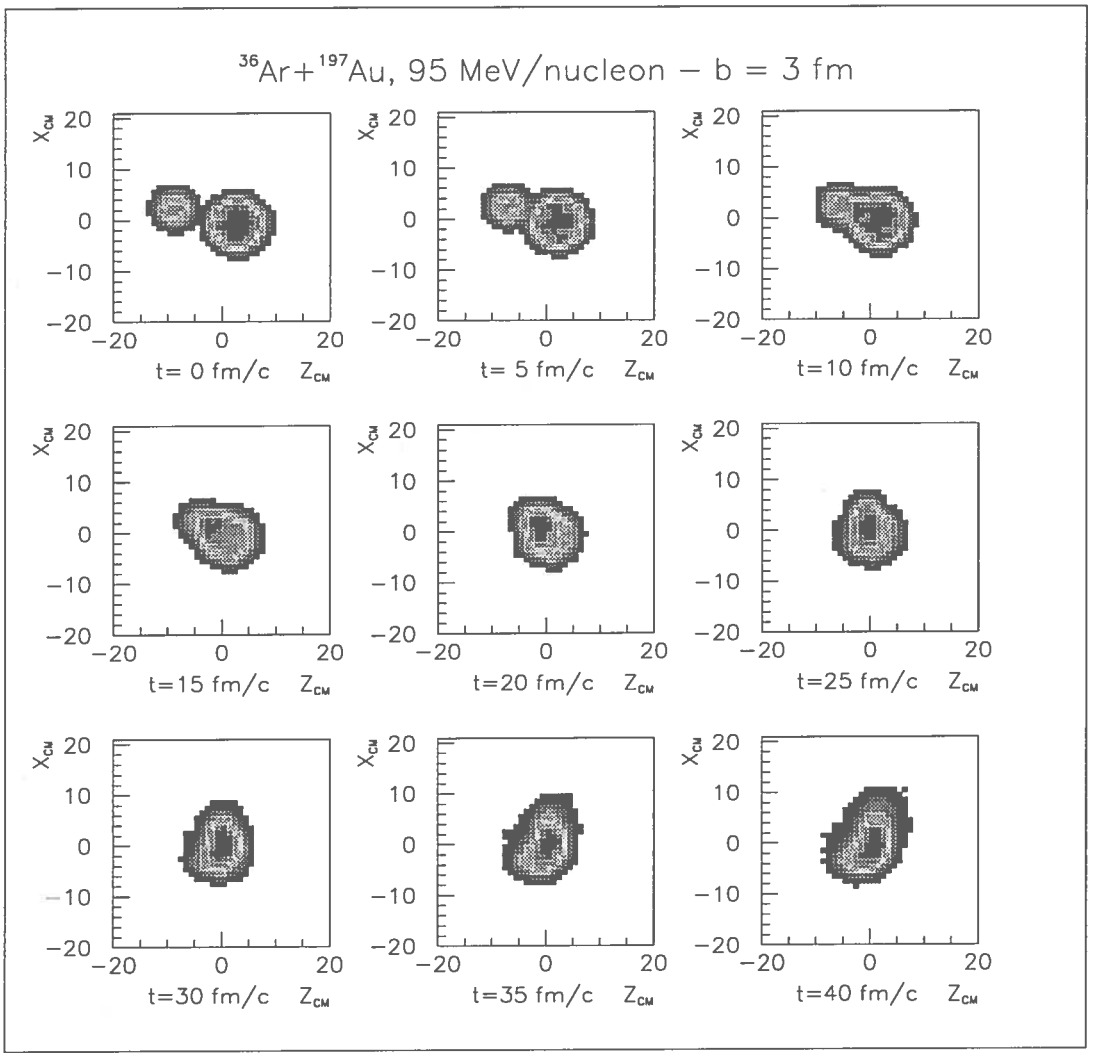

FIG. 23. As fig.22 for $^{36}Ar + ^{197}Au$ system at 95 MeV/nucleon.

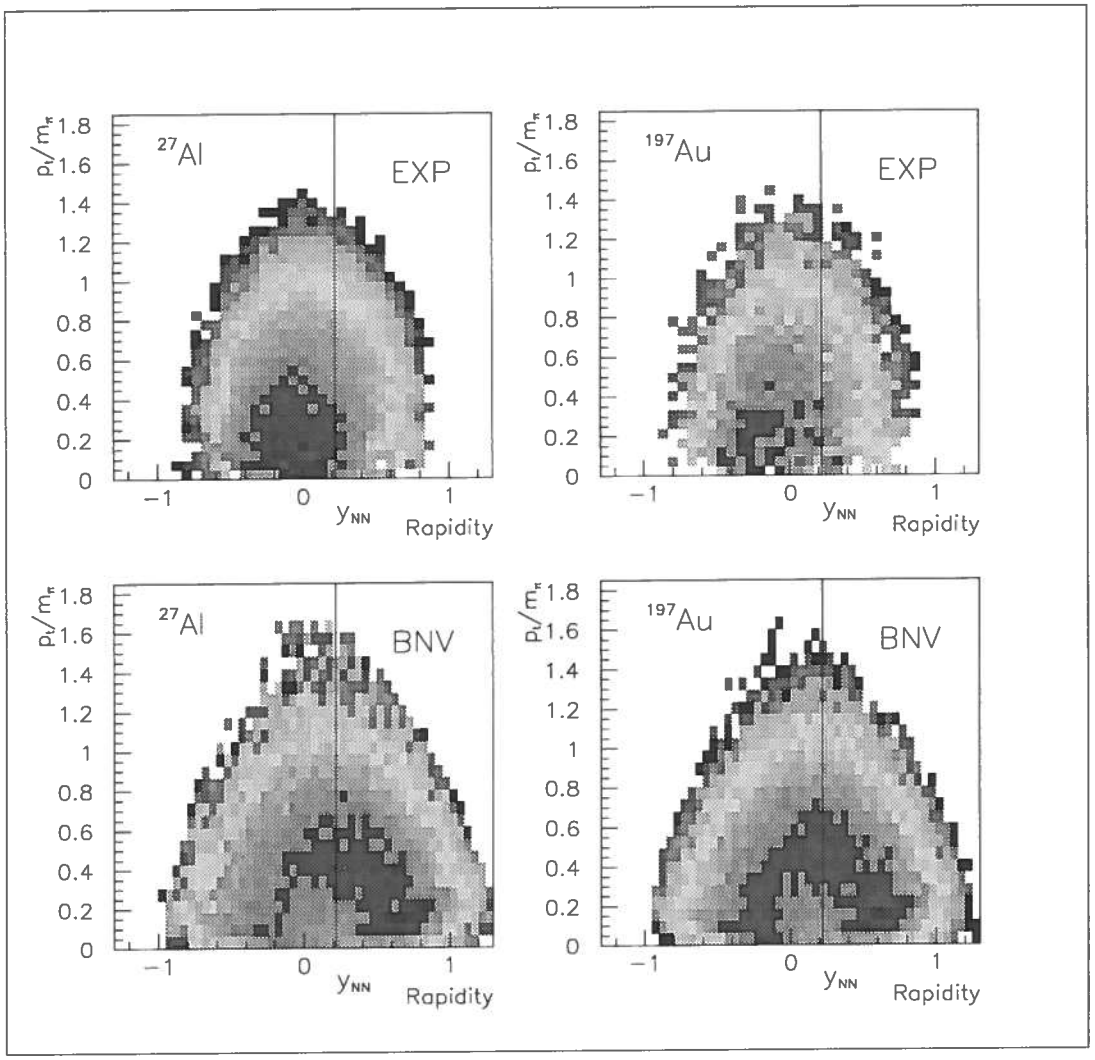

FIG. 24. Experimental (upper panels) and predicted by the BNV calculations (lower panels) pion rapidity plots for $^{36}Ar +^{27} Al$ and $^{36}Ar +^{197} Au$ systems at 95 MeV/nucleon

nuclear medium, and then the shape of the energy spectra and the angular distributions may be considerably distorted. In these last years many inclusive measurements [1,2,31–36] were performed to understand the pion production mechanism and several theoretical works with different physical assumptions, from Fermi boosted NN collisions to coherent mechanisms, were developed [1,2]. Exclusive measurements stressed that most of the collisions producing a pion have a central character [37–40].

Up to now the experimental apparatus have not permitted to have a complete set of data (angular distribution and energy spectra) for pions and hard photons in the same reaction. Moreover, for hard gamma spectra photon background caming from π^o decay grows with increasing bombarding energy. Then, it is important to measure also the π^o cross section to correctly subtract this energy- and angle-dependent component. Moreover, for π° a systematic analysis of the principal characteristic as a function of the target mass was made in measurements that utilized Cherenkov detectors and with a low detection efficiency.

Recently, the construction of big apparatus utilizing BaF_2 detectors, that permit to measure simultaneusly γ and charged particles, has permit to measure hard gamma and π° production with a large efficiency and made semi-exclusive measurements. These measurements have permit to stress the fact that these high energy probes are preferentially emitted in central collisions [27,41] and/or to evidence a certain degree of stopping of projectile for heavy interacting systems in the production of pions [42] and low energy hard gamma [29].

In this paper we present experimental data on inclusive measurements of neutral pions and hard photons produced in reactions induced by a 95 MeV/nucleon ^{36}Ar beam on ^{27}Al, ^{58}Ni, ^{112}Sn, and ^{197}Au targets. The large detector efficiency for π° has permitted to extract informations about the source characteristics as temperature and velocity.

In both cases experimental spectra at different angles were compared with the results of dynamical calculations, based on the numerical solution of the Boltzmann-Nordheim-Vlasov equation (BNV). In case of pions, reabsorption was taken into account on a event-by-event basis.

II. EXPERIMENT AND DATA ANALYSIS

The experiment was performed at GANIL, irradiating ^{27}Al, ^{58}Ni, ^{112}Sn and ^{197}Au targets with a beam of ^{36}Ar at 95 MeV/nucleon. The intensity of the beam was of a few nA for all the targets. The target thicknesses were 1.6, 0.4, 0.8 and 4.1 mg/cm^2, respectively. These values were determined with an uncertainty of 10%. Absolute cross sections were extracted throught the work within $15-20\%$ systematic errors due to beam current and target thickness. Only statistical errors are however taken into account in the drawings.

The employed detector was the multidetector MEDEA [43], coupled to a forward hodoscope of plastic scintillators that covered the angular range from 2.5° to 10°. Data presented in this paper were collected only using the BaF_2 ball of MEDEA, that for this experiment was arranged into 144 modules covering from 42° to 138° in a complete azimuthal geometry. For details on the detection of charged particles see ref. [42]. The hard photon trigger was the minimum bias trigger: events with multiplicity at least two in the whole multidetector (MEDEA + hodoscope). The π° trigger was generated by any twofold coincidence of the BaF_2 detectos associated with 17 MeV γ-equivalent energy threshold.

A typical time resolution of 800 ps FWHM was achieved. The separation of γ-rays from charged particles and neutrons was achieved requiring the proper time of flight and the correct fast/slow ratio in the BaF_2 modules. Energy calibration for photons was made by a 6.13 MeV γ-ray PuC source and the cosmic rays. The most probable energy deposition of cosmic muons was evaluated by the simulation code GEANT3 [44].

Since photons generate an electromagnetic shower, for a correct identification the response of the BaF_2 ball to photons was simulated in Monte Carlo calculations using the code GEANT3 [44]. The algorithm employed for the identification of an electromagnetic shower was the following: all the detectors were associated to a matrix 24*6; if the detector with the highest value of the deposited energy is in the position (i_{max},j_{max}) the energy deposited in all the detectors associated to the positions (i,j), such that $(i_{max}-i)^2+(j_{max}-j)^2 \leq 2$ was summed togheter to have the correct energy of the incoming photon. Moreover, a min-

imum energy of 20 MeV is required in the central module of the cluster. According to Monte Carlo simulations this cut does not affect the meson acceptance but reduces considerably the background due to neutrons.

The photon detection angle is evaluated as the averages of the angles of each fired detectors, weighted over the deposited energy. Due to the large aperture of the detectors ($\Delta\phi = 15°$ and $\Delta\theta \sim 15°$), to smooth the angular distribution the angle of each fired detector was uniformly randomized.

Neutral pions were detected by their main (98.9 %) decay branch into two gamma rays. Invariant mass spectrum have been calculated from pairs of photons using the expression:

$$m_{inv} = \sqrt{2E_1E_2(1 - cos\theta_{12})}. \tag{1}$$

Here, E_1, E_2 and θ_{12} are the energies of each photon and the relative angle between the two showers, respectively. Neutral pions were identified by imposing multiple cuts on the relative angle, on the total energy of the two detected photons and on their invariant mass (see fig. 1). The choice of these cuts was made by the help of GEANT3 simulation. An invariant mass distribution with a resolution of 18% FWHM is obtained as expected from the Monte Carlo simulation (see fig.2), which gives an independent check of the energy calibration.

Pion kinetic energy is obtained by:

$$T_{\pi^\circ} = \sqrt{\frac{2m_\circ^2}{(1 - cos\theta_{12})(1 - X^2)}} - m_\circ \tag{2}$$

where $m_\circ$ is the π° rest mass and $X = (E_1 - E_2)/(E_1 + E_2)$ is the asymmetry parameter.

The pion emission angle is evaluated by

$$cos\theta_{\pi^\circ} = \frac{P_{||}}{P_{tot}} = \frac{E_1 cos\theta_1 + E_2 cos\theta_2}{\sqrt{E_1^2 + E_2^2 + E_1E_2 cos\theta_{12}}} \tag{3}$$

The efficiency of the BaF_2 sphere to the two photon decay of π° as a function of the pion kinetic energy and emission angle was evaluate by a complete GEANT3 simulation where energy threshold and not-working modules (only seven) were taken into account. The effect

of fluctuations in the gain of the single modules was also introduced by a Gaussian spreading around the nominal value of the energy. Also the cuts put to identify pions were taken into account. This efficiency as a function of pion kinetic energy and emission angle is reported in fig.3. All pion data were corrected for this efficiency. Since the efficiency is zero for pion energies greater than 120 MeV, the pion energy spectra are cutted at this value. Using this procedure a realistic energy spectrum both for hard-gamma and for pions is correctly reconstructed [45].

In ref. [46], the interaction of cosmic rays with the experimental setup has been treated by means of a full Monte Carlo simulation with the GEANT3 code and it was evidenced that almost all π°-events recorded in coincidence with zero charged-particle multiplicity can be interpreted as due to cosmic rays. Then the condition that at least a charged particle is detected was imposed to correctly select pions. The same condition was put to sort hard photon spectra.

III. HARD GAMMA RESULTS

For each angle, hard-gamma energy spectra contain a sizeable contamination from π° decay photons. To subtract this component a Monte Carlo simulation has been performed using the π° energy spectra and angular distribution equal to the measured one for the same system. This contamination ranges from 3% to 15% going from 30 MeV to 200 MeV. The uncertainty on this correction, rising with energy, is estimated to be 3-8%.

In fig. 4 for each angle the measured hard-gamma energy spectrum and the contribution from π° decay photons, as obtained from a GEANT3 Monte Carlo simulation is shown for the Sn target. The pion subtracted photon spectra for the four targets at different angles are shown in fig. 5 and 6. Because of the strong contamination of high energy protons at forward angles which is not possible totally eliminate, we preferred to report energy spectra starting from 60°. The values of the double differential cross section for the four targets are reported in Table I.

A systematic analysis was performed on the hard photon spectra to extract various quantities of interest such as the slope parameter, the strength of the dipole component and the source velocity. A simultaneous fit of the double differential cross section was made by the expression proposed in ref. [10], where an exponential energy spectrum and an isotropic+dipolar angular distribution is assumed:

$$\frac{d^2\sigma}{d\Omega dE} = \frac{\sigma_o}{X}\left(1 - \alpha + \frac{\alpha sin^2\theta_{Lab}}{X^2}\right) e^{-XE_{Lab}/E_o} \tag{4}$$

with $X = (1 - \beta cos\theta_{Lab})/\sqrt{1-\beta^2}$, where β is the source velocity, E_o is the inverse slope parameter and α is the relative amplitude of the dipolar component, and σ_{circ} is a normalization factor. Solid lines in figs.5-6 represent the result of the fit.

The values of α, β and E_o parameter within the errors are the same for the four targets (see Table II). The lack of data at forward angles implies that α and β parameter are determined with a large errors. Kept this in mind the value of β about equal to the β_{N-N} (0.22) for all the systems is consistent with the results of ref. [29].

The mean value of E_o (30.2 ± 0.4) is in agreement with the systematics of the inverse slope as a function of the bombarding energy [3]. The values of the strength of the dipole component (α) are in agreement with the values found for different systems and energies (see Table III). The values of ref. [14] are slightly higher, but they are referred at a lower incident energy and the value of this parameter was obtained by setting the source velocity equal to the nucleon-nucleon center-of-mass velocity.

Using the results of the fits for the missing angles and integrating over the energy and the angle, the bremsstrahlung production cross section was found (σ_γ). The values for all the targets are listed in Table IV. The listed errors take into account the statistical error and the extrapolation error that is the principal source of error. In Table IV also the average probability for hard-gamma emission in a single proton-neutron collision within the nuclear medium (p_γ) is reported. Adopting the NN scattering picture [10]:

$$\sigma_\gamma = p_\gamma \sigma_R N_{np} \tag{5}$$

where σ_R is the reaction cross section calculated as in ref. [3]; N_{np} is the number of initial n-p collisions that can be computed with the geometrical equal-participant model [47]. The data of the hard gamma production cross section as a function of $\sigma_R N_{np}$ follow the straight line relationship (fig.7) and by a weighted best fit we found for p_γ the value of $(2.9 \pm 0.2) \cdot 10^{-4}$.

IV. NEUTRAL PION RESULTS

Fig.8 shows pion energy spectra for angles between 0° and 180° for steps of 15° for the gold target. Spectra are, generally, characterized by a maximum around 20-30 MeV and for higher energies by an exponential tail. Similar spectra were obtained for all the targets. In Tab.V the values of the double differential cross section are listed for all the targets.

Solid lines in figure represent the result of a moving source analysis carried out to get the value of the temperature parameter τ and the source velocity $\beta_\circ$. Following the relativistic Maxwell-Boltzmann formula, the energy spectrum in the lab is given by:

$$\frac{d^2\sigma}{d\Omega dE} = pE' \frac{\sigma_\circ}{4\pi m^3} \frac{e^{E'/\tau}}{2\left(\frac{\tau}{m}\right)^2 K_1\left(\frac{m}{\tau}\right) + \left(\frac{\tau}{m}\right) K_0\left(\frac{m}{\tau}\right)} \tag{6}$$

where

$$E' = \frac{E - \beta_\circ p cos\theta}{\sqrt{1-\beta_\circ^2}} \tag{7}$$

is the total energy of the emitted particle in the source frame; E, p and θ are the total energy, the linear momentum and the detection angle in lab system, respectively. K_0 and K_1 are the modified Bessel functions of order 0 and 1 [48]. $\sigma_\circ$ is the production cross section and m is the pion rest mass.

Making a simultaneous fit of the spectra at different angles we get for $\sigma_\circ$, $\beta_\circ$ and τ the values listed in Table VI. Because of the low detection efficiency for high-energy pions at forward angles, we excluded from the fits data relative at angles lower then 30°. We verified that including these angles the values of the fit parameters did not change substantially. The values of $\beta_\circ$ are very low; for heavy targets this value is quite lower than the velocity

of the center of mass. This fact is due to a complex interplay between reabsorption effects and stopping of projectile as it is diffusely discussed in ref. [42].

For the slope parameter we get about the same value of 21 MeV for all the targets. This value is in agreement with the value found for the system $^{16}O+^{27}Al$ at 94 MeV/nucleon [41]. As a consequence of the low neutral pion efficiency in the most part of the previous measurements the slope parameter was extracted making a fit on the energy distribution or on the transverse momentum distribution. A thermal fit of the π° transverse-momentum spectra p_t (fig.9) was made by the expression $d\sigma/dp_t \propto p_t\sqrt{T}\sqrt{m_t}\exp(-m_t/T)$ with $m_t = \sqrt{m^2+p_t^2}$. It gives for T the value of 18 ± 2 MeV for all the targets, in good agreement with the systematic study of pion energy slope of Suzuki et al. [33]. Inverse slope parameter from angle integrated π° spectra have been extracted for the four target fitting the exponential energy distribution with $d\sigma/dE_\pi \propto exp(-E_\pi/E_0)$ (fig.10). The value of E_0 are 14 ± 1 MeV, 16 ± 1 MeV, 11 ± 1 MeV and 15 ± 1 MeV for Al, Ni, Sn, Au targets. These values are very low if compared with the existing E_0 systematics as a function of the bombarding energy [1]. However, it is worth to note that our data are referred to heavy interacting systems for which the final state effects play a relevant role in the modification of the shape of the energy spectrum and this systematics was made for light interacting systems. It gives a mean value of 22 MeV for all the bombarding energies, excluding the very high values obtained in one of the first measurements of subthreshold π° production [49]. Moreover, it is interesting to note that a value of 15 MeV was obtained for E_0 in the reaction $^{12}C+^{12}C$ at 84 MeV/nucleon for π^+ production [38].

Integrating over the energy and the angle we obtained the pion production cross sections listed for the different targets in Table VII. The error due to statistics (not listed) is about $1-2\%$. These values of the cross sections scaled for the factor $(A_pA_t)^{2/3}$ are in good agreement with the systematics on the pion production cross section as a function of the bombarding energy [50]. The mass dependence of the cross section is however not well described by $A_t^{2/3}$ (see third column of Table VII). In general, data for many different systems have shown that the target mass dependence of the total cross section does not

follow a simple power law over the whole mass range: it flattens for heavier targets. This is due to the fact that for heavy interacting systems pion reabsorption effects increase. Our data, as was found for reactions induced by ^{16}O at 95 MeV/nucleon [34], are in good agreement with a dependence of the type $\sigma_{tot} \propto A_p^{1/3}A_t^{2/3} + A_p^{2/3}A_t^{1/3}$ (see fourth column of Table VII). This type of dependence is expected from an extend source formed by the nucleons enclosed in the overlapping volume between the target and the projectile nuclei [50].

As it is well know, the behavior of the pion distributions is strongly affected by the final state interactions. This is obviously more evident for heavy interacting systems. By looking at the pion rapidity distributions for the four targets (see fig.11) as a function of the pion energy, we can note that low energy pions (T_π = 0-20 MeV) are characterized by a nearly symmetric rapidity distribution around y=0, while large rapidities (and then forward peaked distribution) are selected by energetic pion ($T_\pi > 50$ MeV). These features could point out that energetic pions are mainly originated from first NN collisions, while low energy pions could be the result of successive NN collisions. Increasing the target size we note that backward emission is preferred. In fact for the gold target for low energy pions the rapidity distribution is centered at a negative value and for energetic pions it is less forward peaked than for the ^{27}Al. These aspects show the relevance of pion absorption that depends on the pion energy and on the source location. In the next section we will describe a dynamical calculation where we try to proper describe reabsorption effects.

V. ANALYSIS OF THE DATA WITHIN A DYNAMICAL CALCULATION

A. Boltzmann-Nordheim-Vlasov calculations

A dynamical calculation of the collision process was performed by numerically solving the Boltzmann-Nordheim-Vlasov equation [51,52] In a perturbative approach [53] pions and hard gamma were assumed to originate mainly in nucleon-nucleon collisions and the yields are evaluated by incoherent superposition of individual probabilities. For all the targets and

TABLES

TABLE I. Hard gamma double differential cross section $\frac{d^2\sigma}{d\Omega dE}$ $(\frac{\mu b}{srMeV})$ for ^{36}Ar at 95 MeV/nucleon on different targets.

θ_γ	E_γ(MeV)	^{27}Al	^{58}Ni	^{112}Sn	^{197}Au
$60° \div 76°$	35	6.3 ± 0.2	13.4 ± 0.6	20.2 ± 0.5	23.7 ± 0.8
$60° \div 76°$	45	3.6 ± 0.2	8.0 ± 0.5	12.1 ± 0.4	14.9 ± 0.6
$60° \div 76°$	55	2.7 ± 0.2	5.5 ± 0.4	8.3 ± 0.4	10.3 ± 0.5
$60° \div 76°$	65	2.1 ± 0.1	4.9 ± 0.4	7.1 ± 0.3	8.4 ± 0.5
$60° \div 76°$	75	2.1 ± 0.1	3.2 ± 0.3	5.3 ± 0.3	7.0 ± 0.4
$60° \div 76°$	85	1.2 ± 0.1	2.6 ± 0.3	4.7 ± 0.3	5.7 ± 0.4
$60° \div 76°$	95	1.1 ± 0.1	2.3 ± 0.3	3.6 ± 0.2	4.7 ± 0.4
$60° \div 76°$	105	1.0 ± 0.1	2.1 ± 0.2	2.6 ± 0.2	3.4 ± 0.3
$60° \div 76°$	115	0.80 ± 0.09	1.2 ± 0.2	2.1 ± 0.2	3.0 ± 0.3
$60° \div 76°$	125	0.53 ± 0.07	0.9 ± 0.2	1.5 ± 0.1	1.8 ± 0.2
$60° \div 76°$	135	0.31 ± 0.05	0.6 ± 0.1	1.4 ± 0.1	1.4 ± 0.2
$60° \div 76°$	145	0.23 ± 0.05	0.3 ± 0.1	0.8 ± 0.1	1.0 ± 0.2
$60° \div 76°$	155	0.11 ± 0.03	0.4 ± 0.1	0.48 ± 0.08	0.8 ± 0.1
$60° \div 76°$	165	0.15 ± 0.04	0.07 ± 0.05	0.36 ± 0.07	0.4 ± 0.1
$60° \div 76°$	175	0.05 ± 0.02	0.21 ± 0.08	0.18 ± 0.05	0.21 ± 0.07
$60° \div 76°$	185	0.02 ± 0.02	-	0.11 ± 0.04	0.24 ± 0.08
$60° \div 76°$	195	0.03 ± 0.02	0.08 ± 0.05	0.07 ± 0.03	0.07 ± 0.04
$60° \div 76°$	205	-	-	0.04 ± 0.02	-
$60° \div 76°$	215	-	-	0.03 ± 0.02	-
$60° \div 76°$	225	-	-	0.04 ± 0.02	-
$60° \div 76°$	235	-	-	0.03 ± 0.02	-
$76° \div 90°$	35	6.1 ± 0.2	13.4 ± 0.5	18.8 ± 0.4	26.0 ± 0.7
$76° \div 90°$	45	3.6 ± 0.2	8.0 ± 0.4	10.7 ± 0.3	14.8 ± 0.5

$76° \div 90°$	55	2.5 ± 0.1	5.1 ± 0.3	7.7 ± 0.3	10.3 ± 0.4
$76° \div 90°$	65	1.8 ± 0.1	3.4 ± 0.3	5.2 ± 0.2	6.9 ± 0.4
$76° \div 90°$	75	1.19 ± 0.09	2.2 ± 0.2	3.8 ± 0.2	5.1 ± 0.3
$76° \div 90°$	85	0.99 ± 0.08	1.9 ± 0.2	2.7 ± 0.2	3.0 ± 0.2
$76° \div 90°$	95	0.67 ± 0.07	1.5 ± 0.2	2.5 ± 0.2	2.5 ± 0.2
$76° \div 90°$	105	0.55 ± 0.06	0.9 ± 0.1	1.7 ± 0.1	2.3 ± 0.2
$76° \div 90°$	115	0.32 ± 0.05	1.0 ± 0.1	1.1 ± 0.1	1.4 ± 0.2
$76° \div 90°$	125	0.34 ± 0.05	0.5 ± 0.1	0.9 ± 0.1	1.2 ± 0.1
$76° \div 90°$	135	0.18 ± 0.04	0.5 ± 0.1	0.55 ± 0.08	1.0 ± 0.1
$76° \div 90°$	145	0.07 ± 0.02	0.4 ± 0.1	0.39 ± 0.07	0.42 ± 0.09
$76° \div 90°$	155	0.08 ± 0.02	0.21 ± 0.07	0.25 ± 0.05	0.28 ± 0.07
$76° \div 90°$	165	0.05 ± 0.02	0.09 ± 0.05	0.22 ± 0.05	0.12 ± 0.05
$76° \div 90°$	175	0.05 ± 0.02	0.13 ± 0.05	0.15 ± 0.04	0.16 ± 0.05
$76° \div 90°$	185	0.011 ± 0.009	-	0.06 ± 0.03	0.06 ± 0.03
$76° \div 90°$	195	-	-	-	0.06 ± 0.03
$76° \div 90°$	205	-	-	0.05 ± 0.02	0.05 ± 0.03
$76° \div 90°$	215	-	-	0.04 ± 0.02	0.03 ± 0.02
$76° \div 90°$	225	-	-	0.02 ± 0.01	0.05 ± 0.03
$90° \div 104°$	35	4.4 ± 0.2	9.4 ± 0.4	15.2 ± 0.4	22.0 ± 0.7
$90° \div 104°$	45	2.8 ± 0.1	6.8 ± 0.3	9.4 ± 0.3	13.1 ± 0.5
$90° \div 104°$	55	2.0 ± 0.1	4.4 ± 0.3	6.1 ± 0.2	8.4 ± 0.4
$90° \div 104°$	65	1.27 ± 0.09	2.7 ± 0.2	4.5 ± 0.2	6.2 ± 0.4
$90° \div 104°$	75	0.94 ± 0.08	2.7 ± 0.2	3.4 ± 0.2	5.0 ± 0.3
$90° \div 104°$	85	0.85 ± 0.07	2.0 ± 0.2	2.8 ± 0.2	3.4 ± 0.3
$90° \div 104°$	95	0.67 ± 0.06	1.5 ± 0.2	2.1 ± 0.1	3.02 ± 0.3
$90° \div 104°$	105	0.38 ± 0.05	0.9 ± 0.1	1.4 ± 0.1	2.2 ± 0.2
$90° \div 104°$	115	0.32 ± 0.04	0.5 ± 0.1	0.93 ± 0.09	1.5 ± 0.2

$90° \div 104°$	125	0.09 ± 0.03	0.6 ± 0.1	0.78 ± 0.08	1.1 ± 0.2
$90° \div 104°$	135	0.14 ± 0.03	0.37 ± 0.08	0.41 ± 0.06	0.8 ± 0.1
$90° \div 104°$	145	0.09 ± 0.02	0.27 ± 0.07	0.30 ± 0.05	0.8 ± 0.1
$90° \div 104°$	155	0.03 ± 0.01	0.16 ± 0.05	0.21 ± 0.04	0.4 ± 0.1
$90° \div 104°$	165	0.05 ± 0.02	0.13 ± 0.05	0.09 ± 0.03	0.34 ± 0.08
$90° \div 104°$	175	0.03 ± 0.01	0.07 ± 0.04	0.08 ± 0.03	0.07 ± 0.04
$90° \div 104°$	185	0.008 ± 0.007	0.04 ± 0.03	0.15 ± 0.04	0.12 ± 0.05
$90° \div 104°$	195	0.009 ± 0.007	0.10 ± 0.04	0.05 ± 0.02	0.11 ± 0.05
$90° \div 104°$	205	0.014 ± 0.009	0.03 ± 0.02	0.02 ± 0.01	-
$90° \div 104°$	215	-	0.05 ± 0.03	0.03 ± 0.02	-
$90° \div 104°$	225	0.010 ± 0.007	-	0.02 ± 0.01	-
$104° \div 120°$	35	3.5 ± 0.1	8.5 ± 0.4	14.2 ± 0.3	18.4 ± 0.5
$104° \div 120°$	45	2.5 ± 0.1	6.0 ± 0.3	8.7 ± 0.3	11.6 ± 0.4
$104° \div 120°$	55	1.7 ± 0.1	4.1 ± 0.3	6.6 ± 0.2	7.2 ± 0.3
$104° \div 120°$	65	1.35 ± 0.09	2.7 ± 0.2	4.3 ± 0.2	5.0 ± 0.3
$104° \div 120°$	75	1.06 ± 0.08	2.0 ± 0.2	3.5 ± 0.2	3.7 ± 0.2
$104° \div 120°$	85	0.67 ± 0.06	1.6 ± 0.2	2.5 ± 0.2	3.1 ± 0.2
$104° \div 120°$	95	0.53 ± 0.06	1.2 ± 0.2	1.8 ± 0.1	1.7 ± 0.2
$104° \div 120°$	105	0.39 ± 0.05	1.1 ± 0.1	1.6 ± 0.1	1.4 ± 0.1
$104° \div 120°$	115	0.23 ± 0.04	0.6 ± 0.1	0.91 ± 0.09	0.95 ± 0.1
$104° \div 120°$	125	0.13 ± 0.03	0.5 ± 0.1	0.63 ± 0.08	0.7 ± 0.1
$104° \div 120°$	135	0.07 ± 0.02	0.40 ± 0.08	0.36 ± 0.06	0.24 ± 0.07
$104° \div 120°$	145	0.10 ± 0.02	0.18 ± 0.06	0.24 ± 0.05	0.17 ± 0.05
$104° \div 120°$	155	0.03 ± 0.01	0.21 ± 0.06	0.16 ± 0.04	0.12 ± 0.04
$104° \div 120°$	165	0.03 ± 0.01	0.07 ± 0.04	0.09 ± 0.03	0.12 ± 0.04
$104° \div 120°$	175	-	0.06 ± 0.03	0.15 ± 0.04	0.06 ± 0.03
$104° \div 120°$	185	0.02 ± 0.01	0.08 ± 0.04	0.11 ± 0.03	-

$104° \div 120°$	195	-	0.05 ± 0.03	0.04 ± 0.02	-
$104° \div 120°$	205	0.015 ± 0.009	-	0.03 ± 0.02	-
$104° \div 120°$	215	0.02 ± 0.01	-	0.07 ± 0.02	-
$104° \div 120°$	225	-	-	0.03 ± 0.02	-
$120° \div 138°$	35	2.1 ± 0.1	5.7 ± 0.3	9.7 ± 0.3	12.2 ± 0.4
$120° \div 138°$	45	1.8 ± 0.1	3.6 ± 0.3	6.1 ± 0.2	7.0 ± 0.3
$120° \div 138°$	55	1.05 ± 0.08	2.6 ± 0.2	4.2 ± 0.2	5.2 ± 0.3
$120° \div 138°$	65	0.75 ± 0.07	2.4 ± 0.2	3.1 ± 0.2	3.6 ± 0.2
$120° \div 138°$	75	0.67 ± 0.07	1.3 ± 0.2	2.4 ± 0.2	2.5 ± 0.2
$120° \div 138°$	85	0.55 ± 0.06	1.2 ± 0.2	1.5 ± 0.1	2.0 ± 0.2
$120° \div 138°$	95	0.32 ± 0.05	0.7 ± 0.1	1.2 ± 0.1	1.3 ± 0.1
$120° \div 138°$	105	0.22 ± 0.04	0.7 ± 0.1	0.79 ± 0.09	0.7 ± 0.1
$120° \div 138°$	115	0.19 ± 0.03	0.6 ± 0.1	0.64 ± 0.08	0.7 ± 0.1
$120° \div 138°$	125	0.10 ± 0.03	0.34 ± 0.08	0.43 ± 0.06	0.26 ± 0.07
$120° \div 138°$	135	0.07 ± 0.02	0.15 ± 0.06	0.19 ± 0.04	0.22 ± 0.06
$120° \div 138°$	145	0.03 ± 0.01	0.17 ± 0.06	0.19 ± 0.04	0.09 ± 0.04
$120° \div 138°$	155	0.04 ± 0.02	0.16 ± 0.05	0.14 ± 0.04	0.15 ± 0.05
$120° \div 138°$	165	0.011 ± 0.009	0.07 ± 0.04	0.07 ± 0.03	-
$120° \div 138°$	175	-	0.04 ± 0.03	0.08 ± 0.03	0.03 ± 0.02
$120° \div 138°$	185	-	0.11 ± 0.04	0.04 ± 0.02	0.02 ± 0.02
$120° \div 138°$	195	-	-	0.03 ± 0.02	-
$120° \div 138°$	205	-	-	0.04 ± 0.02	-
$120° \div 138°$	215	-	-	0.03 ± 0.01	-

TABLE II. Parameters obtained by least-squares fits to the hard gamma spectra at all angles. Fits were made by formula (4) with all four parameters free.

Target	$\sigma_o(\mu$b/sr MeV)	E_o(MeV)	α	β
^{27}Al	15 ± 2	30 ± 1	0.18 ± 0.12	0.24 ± 0.05
^{58}Ni	31 ± 2	31 ± 1	0.14 ± 0.10	0.14 ± 0.08
^{112}Sn	51 ± 2	30.3 ± 0.5	0.20 ± 0.10	0.19 ± 0.03
^{197}Au	71 ± 4	29.3 ± 0.7	0.18 ± 0.12	0.21 ± 0.05

TABLE III. Strength of the dipole component (α) for different systems and energies.

System	Energy (MeV/nucleon)	α	Ref.
$^{7}Li + Li$	30	0.48 ± 0.09	[14]
$^{7}Li + Pb$	30	0.49 ± 0.10	[14]
$^{20}Ne + Mg$	30	0.32 ± 0.07	[14]
$^{40}Ar + Ca$	30	0.29 ± 0.05	[14]
$^{40}Ar + Pb$	30	0.36 ± 0.06	[14]
$^{86}Kr + C$	44	0.31 ± 0.15	[10]
$^{86}Kr + Ag$	44	0.16 ± 0.09	[10]
$^{86}Kr + Au$	44	0.24 ± 0.06	[10]
$^{86}Kr + Ni$	60	0.15 ± 0.06	[28]
$^{136}Xe + Sn$	89	0.21 ± 0.87	[12]
$^{36}Ar + C$	95	0.14 ± 0.05	[29]
$^{36}Ar + Au$	95	0.15 ± 0.03	[29]
$^{136}Xe + Sn$	124	0.39 ± 0.67	[12]

TABLE IV. Bremsstrahlung cross section and probability for hard gamma emission. Errors take into account uncertainty due to extrapolation.

Target	σ_γ(mb)	$p_\gamma \cdot 10^{-4}$
^{27}Al	2.1 ± 0.3	2.4 ± 0.3
^{58}Ni	4.4 ± 0.5	2.8 ± 0.3
^{112}Sn	7 ± 1	2.9 ± 0.4
^{197}Au	9 ± 1	2.7 ± 0.3

TABLE V. Neutral pion double differential cross section $\frac{d^2\sigma}{d\Omega dE}$ $(\frac{nb}{srMeV})$ for ^{36}Ar at 95 MeV/nucleon on different targets.

θ_γ	E_π(MeV)	^{27}Al	^{58}Ni	^{112}Sn	^{197}Au
$0° \div 15°$	5	117 ± 20	149 ± 47	134 ± 36	379 ± 120
$0° \div 15°$	15	144 ± 25	111 ± 45	152 ± 42	295 ± 122
$0° \div 15°$	25	276 ± 42	258 ± 82	343 ± 77	663 ± 222
$0° \div 15°$	35	194 ± 39	384 ± 122	498 ± 107	694 ± 247
$0° \div 15°$	45	354 ± 63	201 ± 101	709 ± 150	320 ± 185
$0° \div 15°$	55	108 ± 41	472 ± 221	-	-
$15° \div 30°$	5	120 ± 11	100 ± 22	157 ± 22	205 ± 50
$15° \div 30°$	15	197 ± 17	264 ± 41	278 ± 33	390 ± 78
$15° \div 30°$	25	222 ± 19	336 ± 51	360 ± 41	430 ± 92
$15° \div 30°$	35	267 ± 24	349 ± 57	366 ± 46	765 ± 132
$15° \div 30°$	45	229 ± 25	474 ± 78	474 ± 62	474 ± 124
$15° \div 30°$	55	233 ± 29	368 ± 82	406 ± 65	580 ± 153
$15° \div 30°$	65	208 ± 31	220 ± 67	217 ± 50	281 ± 118
$15° \div 30°$	75	49 ± 17	150 ± 68	85 ± 35	171 ± 99
$30° \div 45°$	5	133 ± 9	149 ± 20	194 ± 18	352 ± 49
$30° \div 45°$	15	200 ± 12	246 ± 28	292 ± 24	471 ± 62
$30° \div 45°$	25	245 ± 15	299 ± 34	344 ± 29	712 ± 83
$30° \div 45°$	35	224 ± 15	357 ± 39	372 ± 32	532 ± 76
$30° \div 45°$	45	241 ± 16	238 ± 34	328 ± 32	473 ± 75
$30° \div 45°$	55	191 ± 15	230 ± 36	295 ± 32	354 ± 69
$30° \div 45°$	65	159 ± 15	192 ± 36	308 ± 35	244 ± 64
$30° \div 45°$	75	123 ± 15	132 ± 32	189 ± 32	285 ± 78
$30° \div 45°$	85	84 ± 14	123 ± 34	66 ± 19	108 ± 49
$30° \div 45°$	95	46 ± 12	47 ± 25	31 ± 16	-

$30° \div 45°$	105	-	29 ± 21	10 ± 10	-
$30° \div 45°$	115	-	16 ± 16	-	-
$45° \div 60°$	5	119 ± 7	145 ± 17	193 ± 16	293 ± 39
$45° \div 60°$	15	200 ± 10	278 ± 25	326 ± 22	619 ± 59
$45° \div 60°$	25	206 ± 11	339 ± 30	379 ± 25	513 ± 57
$45° \div 60°$	35	250 ± 12	315 ± 29	371 ± 25	566 ± 62
$45° \div 60°$	45	191 ± 11	269 ± 28	277 ± 22	551 ± 62
$45° \div 60°$	55	153 ± 10	197 ± 25	220 ± 20	363 ± 53
$45° \div 60°$	65	103 ± 9	156 ± 22	176 ± 19	280 ± 48
$45° \div 60°$	75	85 ± 8	103 ± 20	106 ± 16	207 ± 43
$45° \div 60°$	85	42 ± 6	80 ± 18	63 ± 13	105 ± 32
$45° \div 60°$	95	22 ± 5	21 ± 11	25 ± 9	25 ± 18
$45° \div 60°$	105	19 ± 6	27 ± 14	-	50 ± 30
$45° \div 60°$	115	4 ± 3	-	-	-
$60° \div 75°$	5	130 ± 7	179 ± 18	201 ± 15	284 ± 36
$60° \div 75°$	15	177 ± 9	296 ± 24	360 ± 21	464 ± 47
$60° \div 75°$	25	176 ± 9	272 ± 23	372 ± 22	508 ± 50
$60° \div 75°$	35	189 ± 9	251 ± 23	302 ± 20	532 ± 52
$60° \div 75°$	45	129 ± 8	180 ± 20	6.1 ± 0.2	463 ± 49
$60° \div 75°$	55	98 ± 7	136 ± 17	177 ± 15	319 ± 41
$60° \div 75°$	65	72 ± 6	83 ± 14	135 ± 14	139 ± 27
$60° \div 75°$	75	52 ± 5	112 ± 17	85 ± 11	155 ± 31
$60° \div 75°$	85	24 ± 4	35 ± 10	42 ± 8	41 ± 17
$60° \div 75°$	95	12 ± 3	27 ± 9	19 ± 6	22 ± 13
$60° \div 75°$	105	6 ± 2	12 ± 7	-	19 ± 14
$75° \div 90°$	5	119 ± 7	157 ± 16	212 ± 15	329 ± 36
$75° \div 90°$	15	201 ± 9	274 ± 22	336 ± 19	570 ± 49